communications biology
A Nature Portfolio journal

Article

https://doi.org/10.1038/s42003-025-09155-9

Radiotherapy plus neoadjuvant and concomitant IL-13Rα2-directed immunotoxin therapy for diffuse intrinsic pontine glioma

Julian S. Rechberger[1,2], Wouter J. F. Vanbilloen[1,3], Leo F. Nonnenbroich[4,5], Jizhi Ge[1], Randy S. Schrecengost[6], Rachael A. Vaubel[7], Liang Zhang[1] & David J. Daniels[1,2]

Radiotherapy (RT) is the standard-of-care for diffuse intrinsic pontine glioma (DIPG); however, it functions as a palliative treatment. Interleukin 13 receptor subunit alpha 2 (IL-13Rα2) is upregulated in most DIPG tumors, posing a promising therapeutic target. Immunotherapies harnessing IL-13Rα2 to selectively deliver cytotoxic payloads such as pseudomonas exotoxin A (PE) are safe in DIPG patients and efficacious in preclinical disease models. Here, we used DIPG cell lines and mouse models to compare RT alone with RT plus the IL-13Rα2-targeted PE immunotoxin GB13 (IL13.E13K-PE4E). DNA strand breaks were evaluated by γH2AX and apoptosis, as well as other on-target effects, by Western blot and immunofluorescence. Cell viability and colony formation assays delineated cell viability and proliferation. In vivo efficacy was based on survival of mice with orthotopic tumors. Animals received fractionated focal irradiation and neoadjuvant and concomitant GB13 by convection-enhanced delivery. GB13 improved the efficacy of RT in vitro through inhibition of DNA damage repair and convergent modulation of apoptotic signaling. Combined RT and intratumoral administration of GB13 decreased tumor burden and prolonged survival in orthotopic xenograft and genetically engineered mouse models. These findings indicate that RT plus GB13 is well tolerated and effective, informing future investigation of a novel therapeutic approach for DIPG.

Brain tumors are the most common cancer and leading cause of cancer-related death in children less than 15 years of age[1–3]. Among high-grade gliomas (HGG), which account for the majority of malignant tumors within the central nervous system (CNS)[4], diffuse intrinsic pontine glioma (DIPG) is associated with a particularly dismal prognosis[5,6]. The anatomical localization and infiltrative growth pattern limit neurosurgical intervention to biopsy to confirm the diagnosis and facilitate molecular analyses and testing[7–9]. Despite recent advances in our biological understanding of DIPG and other diffuse midline gliomas (DMG), prognosis and therapy have remained virtually unchanged over decades[10,11]. The preservation of an intact blood-brain barrier (BBB) in DIPG poses a significant challenge to drug efficacy[12,13], contributing to the failure of numerous clinical trials of systemically administered therapeutics[14]. Various innovative treatment approaches, including targeted therapies, immunotherapies, convection-enhanced delivery (CED), and focused ultrasound, are in various stages of investigation but have yet to demonstrate benefit[15]. External beam radiation therapy (RT) remains the cornerstone of (palliative) treatment[16].

High-throughput sequencing efforts in patient-derived DIPG tissue have identified interleukin 13 receptor (IL-13R) signaling axis components as promising candidates for targeted therapeutic intervention[17]. Interleukin 13 (IL-13) is a cytokine involved in immune modulation within physiological and tumoral microenvironments, acting through canonical IL-13 receptor subunit alpha 1 (IL-13Rα1) and non-canonical IL-13 receptor subunit alpha 2 (IL-13Rα2)[18]. IL-13 normally binds to IL-13Rα1, forming a

---

[1]Department of Neurologic Surgery, Mayo Clinic, Rochester, MN, USA. [2]Department of Molecular Pharmacology and Experimental Therapeutics, Mayo Clinic, Rochester, M, USA. [3]Department of Neurology, Elisabeth-Tweesteden Hospital, Tilburg, The Netherlands. [4]Hopp Children's Cancer Center Heidelberg (KiTZ), Heidelberg, Germany. [5]Clinical Cooperation Unit Pediatric Oncology, German Cancer Research Center (DKFZ) and German Consortium for Translational Cancer Research (DKTK), Heidelberg, Germany. [6]Targepeutics, Inc., Hershey, PA, USA. [7]Department of Laboratory Medicine and Pathology, Mayo Clinic, Rochester, MN, USA. ✉e-mail: Daniels.David@mayo.edu

receptor dimer with stabilization from IL-4 receptor alpha (IL-4Rα), and activates apoptotic signaling cascades through a caspase-dependent mechanism[19,20]. Conversely, IL-13Rα2 is a decoy receptor that binds IL-13 as a monomer with higher affinity than IL-13Rα1[21], leading to sequestration of IL-13, preventing apoptotic cell death, and promoting tumor cell proliferation and metastasis[22–24]. IL-13Rα2 is notably overexpressed in a significant proportion of HGG, including DIPG[17,25,26], correlating with poor prognosis[20,27]. Given the promise of IL-13Rα2 as a viable therapeutic target, preclinical investigations[17,28–32] and clinical studies[33–39] have explored IL-13Rα2-targeted immunotherapies. With the pressing need for improved DIPG treatments, strategies enhancing the efficacy of existing therapies are urgently needed.

Here, we evaluated the efficacy of combined standard-of-care RT and the IL-13Rα2/PE immunotoxin GB13 (IL13.E13K-PE4E) in a panel of diverse in vitro and in vivo models of DIPG. GB13 is a novel recombinant chimeric immunotoxin that comprises an N-terminal point-mutant IL-13Rα2 targeting moiety fused to a C-terminal full-length point-mutant PE molecule[32,40]. These alterations enhance specificity and binding affinity for IL-13Rα2 while minimizing harm to non-cancerous cells[41–45]. Additionally, PE-based therapies have been reported to sensitize tumor cells to RT[46,47]. Our results demonstrate that GB13 enhances the efficacy of low-dose RT in DIPG cell lines by inhibiting DNA damage repair and inducing apoptosis pathway activation, thereby suppressing clonogenic growth and promoting cell death. Fractionated focal irradiation with neoadjuvant and concomitant CED of GB13 resulted in decreased tumor burden and prolonged survival in both patient-derived orthotopic xenograft (PDOX) and genetically engineered mouse models (GEMM) of DIPG. Collectively, our findings suggest that combined GB13 and RT is well-tolerated and efficacious, warranting further exploration in preclinical and clinical studies for the treatment of DIPG.

Results

IL-13Rα2 expression analysis in pediatric brain tumors

As IL-13Rα2 is virtually absent on normal cells and expressed almost exclusively on tumor cells, we were interested in exploring whether IL-13Rα2 expression correlated with clinical or genomic features in human data sets of pediatric brain tumors. Previous data have shown a correlation between overexpression of IL-13Rα2 mRNA and particularly unfavorable outcomes in DIPG[20,27]. We analyzed multidimensional patient genomics data from pediatric brain tumors within the cBio Cancer Genomics Portal (http://cbioportal.org) and the Open Pediatric Brain Tumor Atlas (OpenPBTA) dataset in PedcBioPortal (https://pedcbioportal.org)[48–51] and found that IL-13Rα2 mRNA expression was highest in pediatric hemispheric HGG, DIPG, and ependymoma, while medulloblastoma and benign tumors had the lowest level of expression (Fig. 1A). Additionally, the frequency of IL-13Rα2 alterations, based on RNA-Seq mRNA expression data, was highest in H3-mutated DMG/DIPG, followed by HGG/astrocytoma and ependymoma (Fig. 1B and Supplementary Fig. 1A). The most frequently mutated DIPG driver gene, H3-3A (previously H3F3A), was found to be one of the highest co-occurring perturbations with IL-13Rα2 and had a significantly higher alteration frequency in IL-13Rα2 altered malignant gliomas: In IL-13Rα2 altered tumors, the H3-3A mutation was present in 33.3% of cases, compared to only 3.5% in IL-13Rα2 unaltered samples ($P \le 0.0001$; Supplementary Fig. 1B). Overall, this data demonstrates that IL-13Rα2 expression stratifies pediatric brain cancer patients, highlighting the utility of IL-13Rα2 as a prognostic biomarker in this patient population, particularly those with DIPG.

To confirm the presence of IL-13Rα2 protein in DIPG patient tissue, we analyzed samples of tumor tissue and matched normal brain tissue from a series of children with clinically and radiographically confirmed DIPG (Fig. 1C and Supplementary Fig. 1D). In both cases, tumor cells were found to have infiltrated throughout the brainstem. Hematoxylin and eosin (H&E) staining confirmed the presence of high-grade histological features, including nuclear atypia, mitoses, endothelial proliferation, and necrosis. Tumor cells demonstrated robust H3K27M-mutant histone expression and loss of trimethylation of histone H3K27 (H3K27me3) by immunohistochemistry (IHC). Moreover, immunohistochemical analysis revealed positive staining for IL-13Rα2 throughout patient tumors, emphasizing its potential significance as a therapeutic target in this challenging disease. Future studies involving IL-13Rα2 spatial proteogenomics of human tissue are needed to further explore possible correlations between IL-13Rα2 expression and clinical or genomic features of DIPG.

In vitro efficacy of GB13 in DIPG cells

To assess the potency and selectivity of IL-13Rα2-targeted therapy in DIPG within the neural environment, GB13 (IL13.E13K-PE4E), an IL-13Rα2/PE immunotoxin, was tested in a panel of primary CNS cells (normal human astrocytes [NHA]) and patient tumor-derived DIPG cell lines (SU-DIPG IV, SU-DIPG XIII, SU-DIPG XVII, and SF8628). Employing a comprehensive 12-point dose-response experimental setup, cells were exposed to increasing concentrations of GB13, ranging from 1 pg/mL to 320 ng/mL. GB13 exhibited a potent response in DIPG cell lines compared to NHA (Supplementary Fig. 1E), with a notable decrease in IC_{50} and an increase in therapeutic index correlated with elevated IL-13Rα2 protein levels in DIPG cells. Compared to NHA ($IC_{50} = 230.68$ ng/mL), SU-DIPG IV had the lowest IC_{50} (65.37 pg/mL; $P = 0.02$) among the cell lines tested, followed by SF8628 (347.02 pg/mL; $P = 0.02$), SU-DIPG XVII (2.29 ng/mL; $P = 0.02$), and SU-DIPG XIII (44.08 ng/mL; $P = 0.07$; Fig. 1D and Supplementary Fig. 1F). Consequently, the therapeutic index of GB13, which was computed based on the ratio of IC_{50} in NHA to that in individual DIPG cell lines, was most pronounced for SU-DIPG IV (8206.99), followed by SF8628 (727.35), SU-DIPG XVII (119.96), and SU-DIPG XIII (4.96; Supplementary Fig. 1G). To validate these findings on the IL-13Rα2 transcript level, we performed RNA-Seq on a large cohort of patient-derived DIPG and hemispheric HGG cell lines and correlated the expression of IL-13Rα2 mRNA with the therapeutic index of each individual cell line. RNA-Seq analysis showed that IL-13Rα2 mRNA was expressed at levels greater than 1 transcript per million (TPM) in all tumor specimens studied, except for SU-DIPG XIII (0.48 TPM; Supplementary Fig. 1C). Consistent with the results of the DIPG therapeutic indices when compared to IL-13Rα2 protein by Western blot, non-linear least-squares curve fitting showed a strong positive correlation between IL-13Rα2 gene expression and the therapeutic index of GB13 ($r^2 = 0.90$; Fig. 1E). These findings underscore the selective cytotoxicity of GB13 against HGG cell lines, including DIPG, in a manner closely associated with IL-13Rα2 expression.

Sensitization of DIPG cells to RT by GB13

To determine the combinatorial effect of GB13 and the current standard treatment for DIPG, the impact of GB13 on radiation sensitivity was assessed in clonogenic survival assays. Cotreatment of SF8628 cells with GB13 sensitized them to RT across multiple radiation doses (0 Gy, 2.5 Gy, 5 Gy, 7.5 Gy, and 10 Gy; Fig. 2A). Fitting the curves to a linear-quadratic (LQ) model, α and β values for RT alone and RT plus 30 pg/mL of GB13 were $\alpha = 0.063$, $\beta = 0.065$ (α/β ratio = 0.97) and $\alpha = 0.499$, $\beta = 0.037$ (α/β ratio = 13.62), respectively. With 100 pg/mL and 300 pg/mL of GB13 cotreatment, α values increased to 0.943 (14.97-fold) and 1.255 (19.92-fold), respectively. The survival curves with 100 pg/mL and 300 pg/mL GB13 cotreatment did not exhibit a shoulder, and hence β values approached zero and could not be accurately determined. Additionally, the Sensitizer Enhancement Ratio at 10% survival (SER10) was calculated as the ratio of lethal dose at 10% survival (LD10) without drug to LD10 with drug, which demonstrated an increase with escalating concentrations of GB13. With GB13 cotreatment, the SER10 was 1.46, 2.01, and 2.59 for 30 pg/mL, 100 pg/mL, and 300 pg/mL, respectively. Similarly, 30 pg/mL, 100 pg/mL, and 300 pg/mL GB13 led to a 2.47-fold, 5.22-fold, and 9.60-fold reduction in survival versus RT alone at 2.5 Gy, respectively. GB13 treatment alone was similar to vehicle control at the tested concentrations (plating efficiency [PE]: 0.448 ± 0.182, 0.402 ± 0.153, 0.328 ± 0.127, and 0.197 ± 0.068, for 0 pg/mL, 30 pg/mL, 100 pg/mL, and 300 pg/mL GB13 respectively; $P = 0.62$; normalized to 1 in the clonogenic curves). Finally, the synergistic cytotoxic

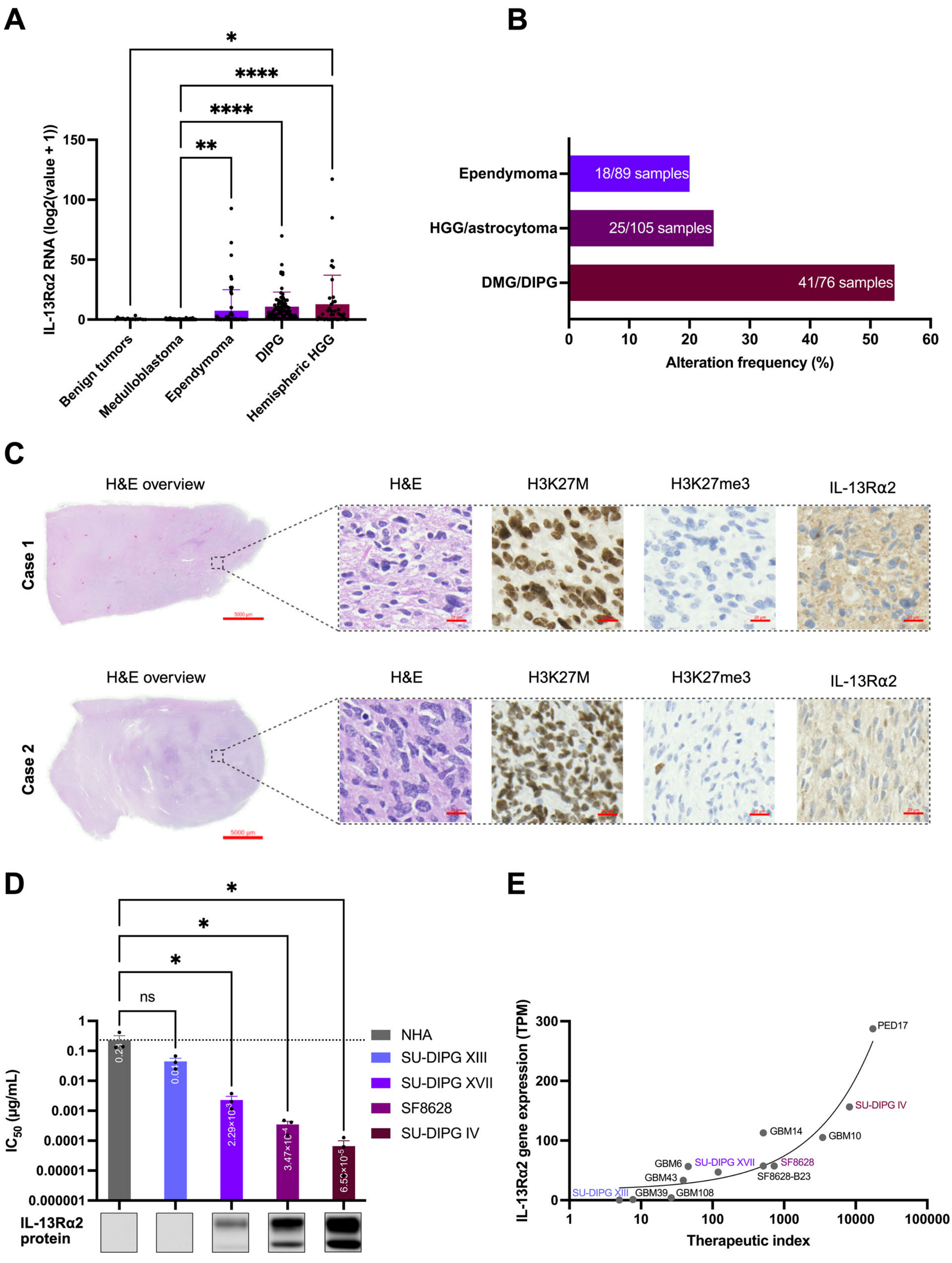

effect of GB13 and RT was determined as the excess of observed effect over expected effect calculated by multiple pharmacological reference models (synergy scoring models), which make different assumptions regarding the expected combination effect[52–57]. Summary synergy scores were computed by averaging the excess response due to treatment interactions above expectation, with resulting values of larger than 10 in all reference models indicating a high degree of formal synergy between GB13 and RT in DIPG cells (Table 1).

After delineating the combined impact of GB13 and RT on clonogenic survival, we assessed the ability of this radio-immunotherapy to alter DIPG colony formation and proliferation (Fig. 2B)[58]. Consistent with inherent sensitivity to ionizing radiation in SF8628, 4 Gy RT decreased clonogenic

Fig. 1 | Targeting interleukin 13 receptor subunit alpha 2 (IL-13Rα2) for immunotoxin therapy in diffuse intrinsic pontine glioma (DIPG). **A** Computational genomic analysis of patient tissue from diverse childhood brain tumors reveals a spectrum of IL-13Rα2 gene expression levels (benign tumors, n = 14; medulloblastoma, n = 122; ependymoma, n = 60; DIPG, n = 76; hemispheric high-grade glioma (HGG), n = 41). Y-axis shows log2(x + 1) transformed RSEM normalized counts. The normalize Quantiles method was applied and the median log2 relative abundance was calculated for each sample and normalized to a common median of 0[1,2]. Data represent the mean ± SD of individual patient samples. Statistical significance denoted as *: P ≤ 0.05; **: P ≤ 0.01; ****: P ≤ 0.0001; analyzed via one-way ANOVA. **B** Genomic analysis of patient tissue showing the frequency of IL-13Rα2 alterations based on RNA-Seq mRNA expression data in H3-mutated diffuse midline glioma (DMG)/DIPG, HGG/astrocytoma, and ependymoma. Total number of patient samples: n = 270. Data sourced from the cBio Cancer Genomics Portal (http://cbioportal.org) and the Open Pediatric Brain Tumor Atlas (OpenPBTA) dataset in PedcBioPortal (https://pedcbioportal.org)[1–5]. **C** Hematoxylin and eosin (H&E) staining alongside immunohistochemistry (IHC) images from DIPG specimens obtained post-mortem, with higher magnification insets of highlighted tumor regions demonstrating robust IL-13Rα2 staining. Scale bars: 1×: 5000 µm, 20×: 20 µm. (**D**) GB13 (IL13.E13K-PE4E) shows a potent response in DIPG cell lines compared to non-cancerous cells of the central nervous system. Results are the mean ± SEM of 3 independent dose-response cell viability experiments. ns: P ≥ 0.05; *: P ≤ 0.05; one-way ANOVA. See Supplementary Fig. 1F for full immunoblot of IL-13Rα2 protein data. NHA, normal human astrocytes. **E** Non-linear least-squares curve fitting illustrating a robust positive correlation between IL-13Rα2 gene expression and GB13 sensitivity, observed across high-grade glioma cell lines, including DIPG. R squared = 0.90.

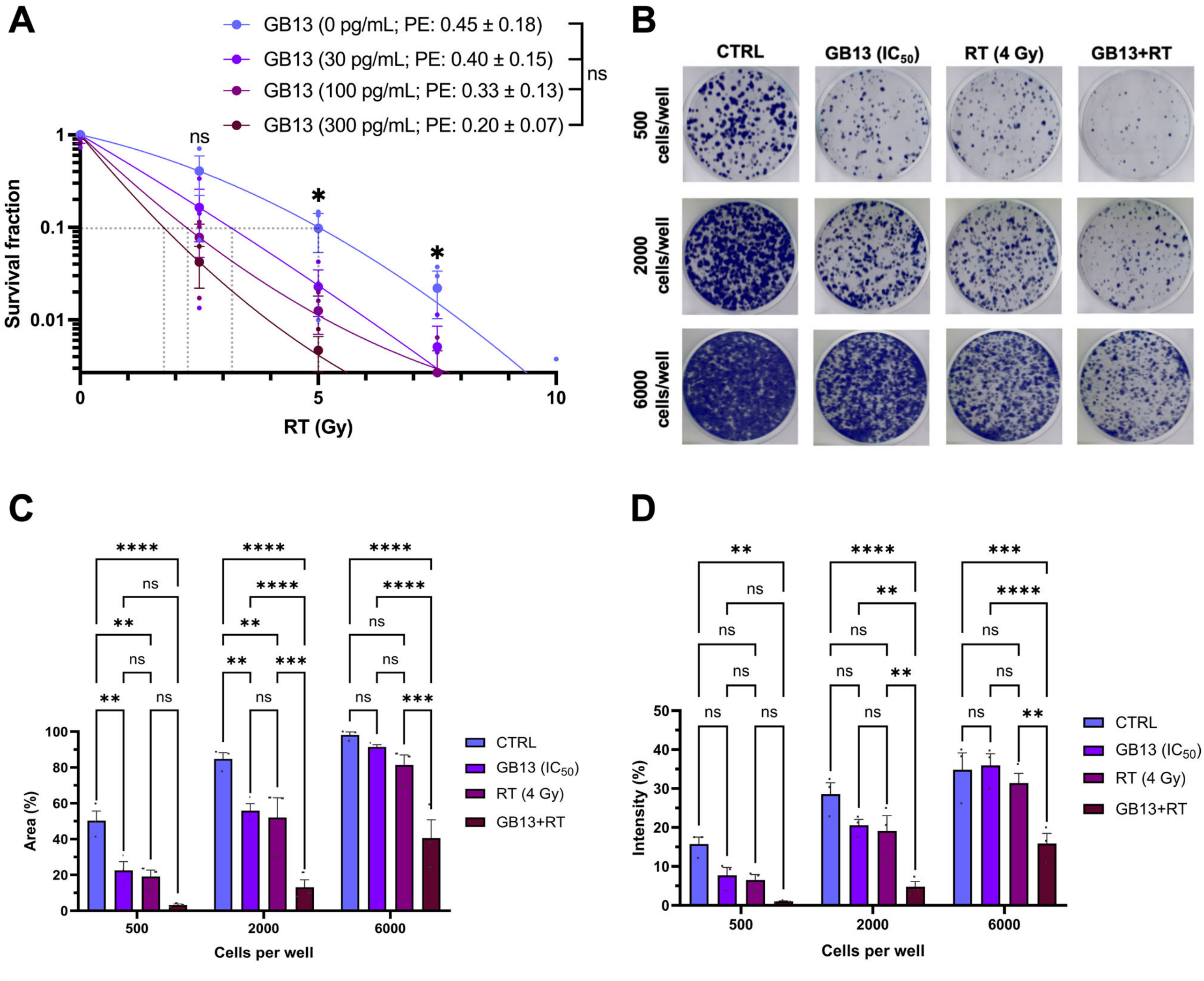

Fig. 2 | GB13 sensitizes DIPG cells to radiotherapy (RT). **A** Clonogenic survival assay conducted on SF8628 cells treated with vehicle control, GB13 at concentrations of 30 pg/mL, 100 pg/mL, or 300 pg/mL GB13 for 24 h prior to RT followed by 48 h post-RT incubation, rinsed with PBS, media changed, and incubated for colony formation. Results are the mean ± SEM of three independent experiments fitted to the linear quadratic (LQ) model. ns: P ≥ 0.05; *: P ≤ 0.05; unpaired t test. **B** Scanned and digitalized images of a 6-well plate illustrating variable colony formation levels of SF8628 cells subjected to the described treatment regimen: vehicle control, GB13 monotherapy at IC_{50}, 4 Gy of RT alone, or GB13 at IC_{50} plus 4 Gy RT. Image data were analyzed using ColonyArea software to determine **C** colony area percentage and **D** colony intensity percentage[6]. Results are the mean ± SEM of 3 independent experiments. ns: P ≥ 0.05; **: P ≤ 0.01; ***: P ≤ 0.001; ****: P ≤ 0.0001; two-way ANOVA.

confluency (Fig. 2C and Supplementary Fig. 2A) and intensity (Fig. 2D and Supplementary Fig. 2B) compared with control, although the significance of these findings varied depending on the seeding density of SF8628 cells (250 to 6000 cells/well). Similar results were observed when cells were exposed to GB13 at IC_{50}, with no significant difference between either monotherapy under any tested conditions (P ≥ 0.05; Fig. 2C, D). However, combined treatment with GB13 at IC_{50} and 4 Gy RT significantly reduced both the confluency (P = 0.0003 for 250 cells/well and P ≤ 0.0001 for 500, 1000, 2000, 4000, and 6000 cells/well; Supplementary Fig. 2A) and intensity (P = 0.0129 for 250 cells/well, P = 0.0002 for 500 cells/well, and P ≤ 0.0001 for 1000, 2000, 4000, and 6000 cells/well; Supplementary Fig. 2B) of clones compared to the vehicle controls. Clonogenic analyses conducted on SU-DIPG IV cells mirrored the findings observed in SF8628 cells regarding both colony area (Supplementary Fig. 2C) and colony intensity (Supplementary Fig. 2D) across the range of seeding densities examined (500–20,000 cells/well). Together, these results indicate that cotreatment with GB13 sensitizes DIPG cells to RT, with increasing concentrations of GB13 correlating with enhanced sensitivity, suggesting a potentiation of RT-induced killing by GB13.

In vitro efficacy and selectivity of combined GB13 and RT

The response to treatments involving GB13 monotherapy, RT alone, and their combined application was evaluated in DIPG cell lines with varying levels of IL-13Rα2 protein (SU-DIPG XIII, SU-DIPG XVII, SF8628, and SU-DIPG IV). Treatment at IC_{50} concentrations for each cell line with GB13 alone (ranging from 65.37 pg/mL to 44.08 ng/mL), RT alone (from 2.5 Gy to 5 Gy), or the combined therapy (GB13 plus RT) did not induce significant alterations in the protein levels of IL-13Rα1, IL-13Rα2, or characteristic histone markers associated with DIPG, such as H3K27M and H3K27me3 ($P \geq 0.05$; Fig. 3A and Supplementary Fig. 2E-H). An exception was noted for IL-13Rα2 in SF8628, where a significant reduction was observed with GB13 treatment ($P = 0.0084$), which was largely counteracted upon the addition of RT ($P = 0.11$).

Table 1 | In vitro synergy analysis of combined GB13 and RT

Reference model (synergy scoring model)	Synergy Score Summary	Score Statistic (p value)
Bliss model[1]	15.40	0.02
Loewe additivity model[2]	10.76	<0.0001
Highest Single Agent (HSA)[3]	20.87	0.001
Zero Interaction Potency (ZIP)[4]	14.29	0.02

Synergy calculations of GB13 and RT in SF8628 cells were performed using SynergyFinder (http://synergyfinder.org), an interactive web-application for analyzing and visualizing multi-treatment multi-dose combination response data[5,6].

GB13 markedly decreased the presence of c-Myc, a protein with rapid turnover, presumably due to the disruption of protein synthesis by the PE-domain of GB13 ($P = 0.008$ in SU-DIPG XIII, $P = 0.024$ in SU-DIPG XVII, and $P = 0.029$ in SU-DIPG IV; Fig. 3B). While RT elevated c-Myc protein levels, this effect was mitigated by combined GB13 and RT treatment ($P = 0.015$ in SU-DIPG XVII, $P = 0.026$ in SU-DIPG IV, and $P \geq 0.05$ in SU-DIPG XIII and SF8628; Supplementary Fig. 2I). GB13 was similarly effective at suppressing the antiapoptotic protein Mcl-1 in all tested cell lines ($P = 0.0023$ in SU-DIPG XIII, $P = 0.002$ in SU-DIPG XVII, $P = 0.0009$ in SF8628, and 0.0035 in SU-DIPG IV). Treatment with combined GB13 and RT further enhanced this response ($P = 0.0005$ in SU-DIPG XIII, $P = 0.0002$ in SU-DIPG XVII, $P \leq 0.0001$ in SF8628, and 0.0009 in SU-DIPG IV; Supplementary Fig. 2J), and increased the proapoptotic Bcl-2 family protein Bak in some cell lines ($P = 0.0039$ in SU-DIPG XIII and $P = 0.0419$ in SF8628; Supplementary Fig. 2K).

Despite redundancies in upstream signaling, cotreatment of GB13 and RT significantly increased protein levels of cleaved caspase 3 ($P \leq 0.0001$ in SU-DIPG XIII, $P = 0.0008$ in SU-DIPG XVII, and $P = 0.0004$ in SF8628) and cleaved PARP-1 ($P \leq 0.0001$ in SU-DIPG XIII, $P = 0.0004$ in SU-DIPG XVII, and $P = 0.0005$ in SF8628; Fig. 3B). However, the impact on cleaved

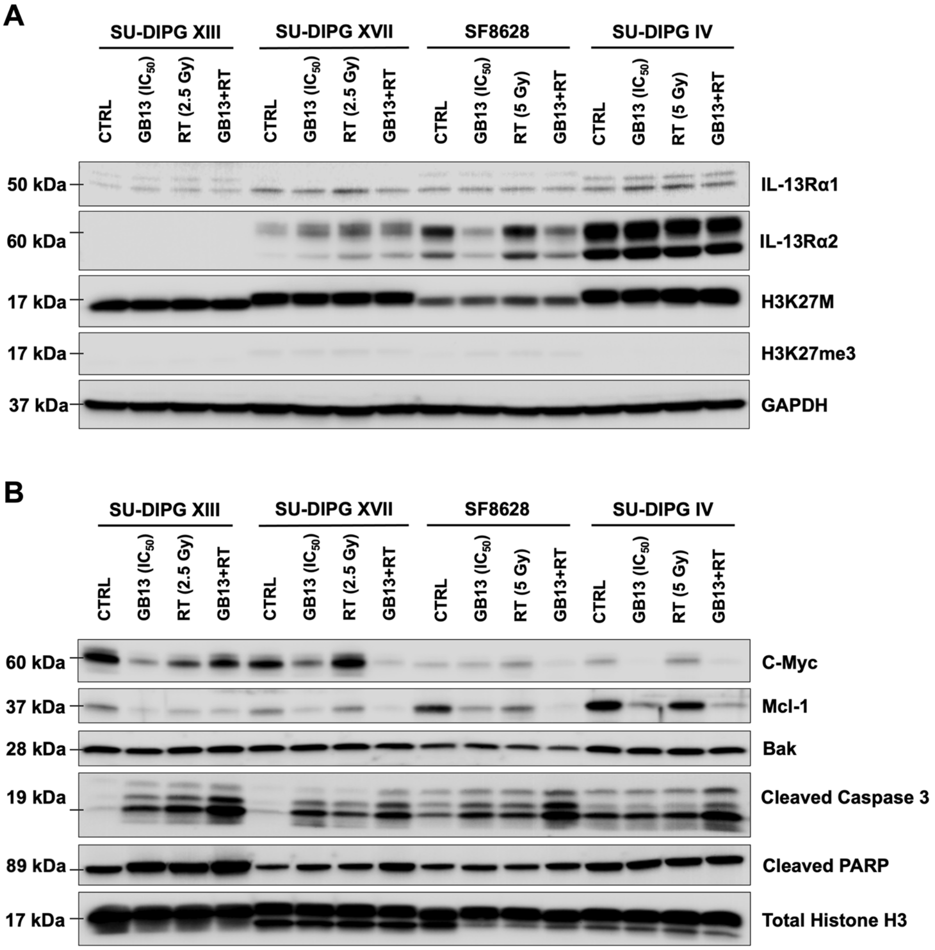

Fig. 3 | Synergistic efficacy and selectivity of combined RT and GB13 in vitro. **A**, **B** Western blot of DIPG cell lines with increasing IL-13Rα2 expression (SU-DIPG XIII, SU-DIPG XVII, SF8628, and SU-DIPG IV) treated for 72 h with vehicle control, GB13 alone at IC_{50}, RT alone, or RT plus GB13 at IC_{50} (added 24 h pre-RT). **A** GAPDH and **B** Total Histone H3 are the loading controls.

caspase 3 did not reach significance (P = 0.14; Supplementary Fig. 2L), and the effect was less pronounced on PARP-1 (P = 0.02; Supplementary Fig. 2M) due to relatively high baseline signaling associated with apoptotic cell death in untreated SU-DIPG IV cells. These data confirm inhibition of protein synthesis by PE immunotoxins such as GB13 and highlight a robust apoptotic response elicited by the combined treatment of GB13 and RT, despite some variation in signaling among DIPG cell lines.

Attenuation of DNA damage repair by GB13 in combination with RT

To further delineate the effects of GB13 on response to radiation, we examined phosphorylated serine-139 on histone variant H2AX (pH2AX-Ser139 also known as γH2AX) foci, which are indicative of DNA damage repair activation[59], in SF8628 cells treated with either vehicle control, GB13 alone, RT alone, or the combination of GB13 and RT. Utilizing a fluorescence-based assay (Supplementary Fig. 3A), RT treatment led to increased levels of γH2AX foci, which was further enhanced by cotreatment with GB13. Notably, pretreatment with GB13 for 24 h prior to RT enhanced the extent of γH2AX foci observed at 1 h, 4 h, and 24 h after RT treatment (Fig. 4A and Supplementary Fig. 3B). While GB13 monotherapy exhibited no substantial difference from vehicle control and RT alone rapidly induced γH2AX foci formation that was mostly resolved within 24 h, GB13 cotreatment significantly increased the number of γH2AX foci per cell 24 h after RT from 4.41 ± 0.62 to 12.7 ± 1.18 (P = 0.0001) for SF8628 cells compared to RT treatment alone, indicating that combined GB13 alters DNA damage response kinetics by attenuating repair mechanisms induced by RT (Fig. 4B).

To corroborate these findings across various DIPG cell lines with distinct molecular characteristics including IL-13Rα2 protein levels (SU-DIPG XIII, SU-DIPG XVII, SF8628, and SU-DIPG IV), we conducted analogous experiments and assessed γH2AX as well as cleaved PARP-1 protein levels. Western blot analysis revealed time- and treatment-dependent implications of GB13 and RT treatments on DNA damage repair and apoptosis induction (Fig. 4C–F). Although there were some variations in γH2AX response among cell lines, pretreatment with GB13 significantly increased γH2AX levels within 1 h after RT (P = 0.0041 in SU-DIPG XIII, P = 0.008 in SU-DIPG XVII, P = 0.0019 in SF8628, and 0.0016 in SU-DIPG IV; Supplementary Fig. 3C–F). The combination of GB13 and RT significantly augmented cleaved PARP-1 levels at the 1-h time point, when signal for γH2AX was at the peak (P = 0.037 in SU-DIPG XVII and 0.026 in SU-DIPG IV), or at the 24-h time point (P = 0.0002 in SU-DIPG XIII and P = 0.0076 in SF8628) compared to RT treatment alone (Supplementary Fig. 3C–F). This increase in the fraction of RT-exposed cells displaying sustained γH2AX elevation with GB13 cotreatment suggests that GB13 enhances RT-induced DNA damage by impeding DNA repair, thereby potentially amplifying apoptosis signaling triggered by either GB13 or RT when employed individually (Supplementary Fig. 4).

In vivo efficacy of combined GB13 and RT

The radiosensitizing effects of GB13 were further evaluated in orthotopic tumors established in athymic nude mice using the SU-DIPG XVII cell line, which exhibits medium levels of IL-13Rα2 protein (SU-DIPG XVII PDOX). To enhance the translational potential of our studies, we sought to develop a clinically relevant dosing regimen of combined fractionated focal irradiation[60,61] with neoadjuvant and concomitant GB13. Due to the large size of GB13 (79 kDa) and to achieve adequate drug distribution and sustained therapeutic effect, we opted for a locoregional drug delivery approach using continuous (7-day) CED into the pons[62]. The efficacy of GB13 (5 µg/mL), RT (5 × 2 Gy delivered through opposed lateral beams with a 15-mm collimator), or combined RT with GB13 (initiated 2 days prior to RT), 70 days after tumor cell inoculation, was evaluated with time to reach a moribund state as primary end point (Fig. 5A). Initially, the efficacy of GB13 monotherapy was established in a pilot experiment to define a therapeutic window for GB13 via CED, whereas 5 µg/mL of GB13 demonstrated a significant survival benefit (median survival of 225 days versus 108 days with vehicle control; P = 0.01; Supplementary Fig. 5A) and durable pharmacodynamic effects in immunohistochemical analyses (Supplementary Fig. 5B). In the extended combination study, combined GB13 and RT resulted in significant survival prolongation (median survival of >350 days [i.e., all animals alive at the end of the study] versus 225 days with GB13 alone and 170 days with RT alone; P = 0.003 and P = 0.006, respectively; Fig. 5B and Table 2). Both GB13 alone and the combinatorial regimen extended survival compared with vehicle control/sham-RT (median survival of 109 days; P = 0.0001 for GB13 alone and P = 0.005 for combined GB13 plus RT), while RT alone did not achieve a significant survival benefit (P = 0.06).

Pharmacodynamic responses within the brains/tumors were analyzed for all treatment cohorts. Administration of fractionated RT (5 × 2 Gy) alongside neoadjuvant and concomitant GB13 (5 µg/mL) substantially reduced the tumor burden at the drug infusion site (H&E overview and high-power images; Fig. 5C). Residual tumor cells exhibited reduced staining for H3K27M and Ki-67 (Fig. 5C and Supplementary Fig. 7A), as determined by IHC, consistent with previous studies. Conversely, there was an elevation in H3K27me3 levels, while the presence of IL-13Rα2 was comparable to that of control animals (Fig. 5C). Monotherapies involving either GB13 or RT demonstrated similar trends to the combined treatment, albeit to a lesser degree, with gross histological examination revealing substantial residual tumors on H&E (overview and high-power images; Fig. 5C). A considerable cell population in tumors treated with GB13 alone and RT alone stained positively for cleaved caspase 3 (Fig. 5C and Supplementary Fig. 7B), suggesting ongoing apoptotic activity not evident in controls. No CD68+ immune cell infiltration was detected in any of the study groups, and no signs of radiation necrosis, neuronal cell death in the contralateral brainstem or surrounding brain regions (NeuN+ cells), or other histopathological abnormalities were observed in the brain tissue sections from either treatment group (Fig. 5C).

To assess the impact of this radio-immunotherapy on tumor burden and survival in an immunocompetent animal model, we utilized a spontaneous brainstem glioma mouse model characterized by mutations in H3F3A-, TP53-, and PDGFRA genes (H3.3 K27M;PDGFRA;p53^{cKO} GEMM) and IL-13Rα2 levels comparable to SU-DIPG XVII[63]. In line with previous reports, ~25% of animals exhibited MRI-detectable tumors outside the hindbrain prior to treatment initiation, with each animal harboring between 1 to 3 such tumors[62,63]. Mice were again treated under 4 separate conditions: vehicle control/sham-RT, GB13 (5 µg/mL), RT (5 × 2 Gy), or combined RT with GB13 (initiated 2 days before RT), 70 days after tumor induction (Fig. 6A). Consistent with observations in SU-DIPG XVII PDOX mice, the most effective concentration for GB13 monotherapy was 5 µg/mL, as evidenced by a median survival of 99.5 days compared to 81.5 days with vehicle control (P = 0.008; Supplementary Fig. 6A) and durable pharmacodynamic responses (Supplementary Fig. 6B) in an initial pilot experiment. In the combination study, the combined treatment of GB13 and RT significantly prolonged survival compared to RT alone (median survival of 110 days and 91 days, respectively; P = 0.0006), but no significance was reached compared to GB13 alone (median survival of 99.5 days; P = 0.47; Fig. 6B and Table 2). Both GB13 alone and the combination therapy extended survival compared to the vehicle control/sham-RT group (median survival of 81.5 days; P = 0.008 for GB13 alone and P ≤ 0.0001 for combined GB13 plus RT), and RT alone did not significantly extend survival (P = 0.17). Pharmacodynamic effects within brains/tumors from each treatment group largely mirrored findings in SU-DIPG XVII PDOX mice (Fig. 6C and Supplementary Fig. 7C, D), with the exception of scattered CD68+ immune cells observed across all cohorts (Supplementary Fig. 7E). Furthermore, multiple additional tumors were evident throughout the brains beyond the region treated by CED (Supplementary Fig. 7F), likely originating at a later stage after tumor induction and contributing to the diminished survival benefit achieved by combined GB13 and RT compared to GB13 alone in the GEMM.

Collectively, these data demonstrate that the combination of fractionated focal irradiation with neoadjuvant and concomitant GB13 is a feasible and safe treatment strategy that offers a considerable survival prolongation

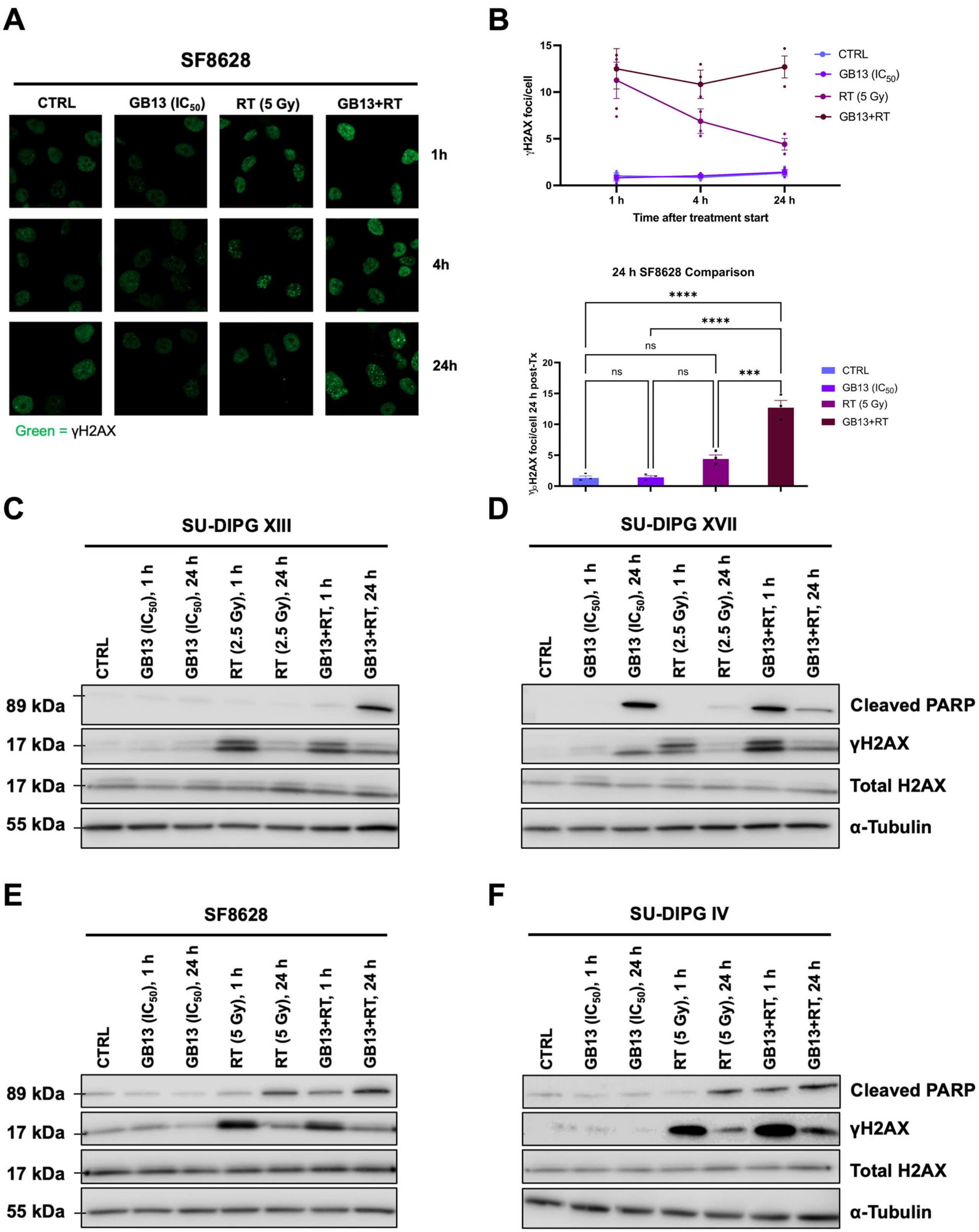

Fig. 4 | GB13 enhances DNA damage in DIPG cells when combined with RT. **A** Representative confocal microscopy images of γH2AX foci in SF8628 cells treated with vehicle control, GB13 alone at IC_{50}, 5 Gy of RT alone, or 5 Gy RT plus GB13 at IC_{50} (added 24 h pre-RT) for 1 h, 4 h, or 24 h. **B** Corresponding quantification of γH2AX foci per SF8628 cell for the different treatment conditions and time points (top), and endpoint analysis at 24 h post-RT or GB13 monotherapy (bottom). Results are the mean ± SEM from 3 independent experiments. ns: $P \geq 0.05$; ***: $P \leq 0.001$; ****: $P \leq 0.0001$; one-way ANOVA. For each group, > 300 nuclei were counted. Western blot analysis of the time- and treatment-dependent implications of GB13 alone, RT alone, or RT plus GB13 at IC_{50} (added 24 h pre-RT) on DNA damage repair and apoptosis induction in (**C**) SU-DIPG XIII, (**D**) SU-DIPG XVII, (**E**) SF8628, and (**F**) SU-DIPG IV cells. Samples were collected 1 h and 24 h after treatment start. α-Tubulin serves as loading control. Results are representative of 3 independent experiments.

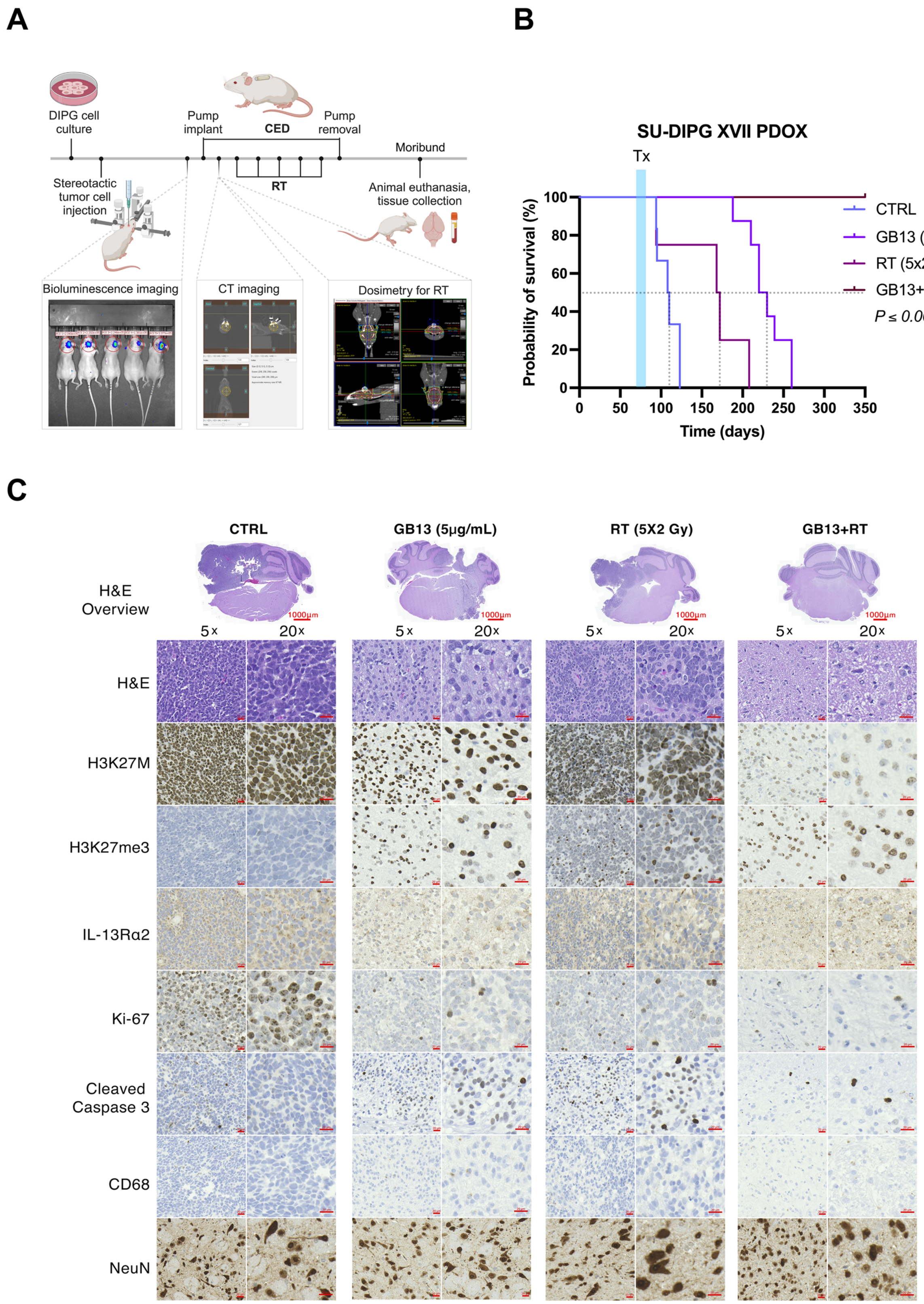

Fig. 5 | Concomitant convection-enhanced delivery (CED) of GB13 plus fractionated RT improves the efficacy of either monotherapy alone in a patient-derived orthotopic xenograft (PDOX) DIPG mouse model. **A** Schema for in vivo efficacy (survival) experiments in PDOX of DIPG. Created in BioRender. Rechberger, J. (2025) https://BioRender.com/vp02r36. **B** Kaplan–Meier graph for mice (n = 4–8 per group) bearing SU-DIPG XVII orthotopic xenografts, treated with 7-day continuous CED of GB13 alone (5 μg/mL; purple curve), RT alone (2 Gy once per day for 5 consecutive days; wine-red curve), or the combination of GB13 plus RT (brown curve), compared with vehicle-treated controls (blue curve). $P \leq 0.0001$; Log-rank (Mantel-Cox) test. Tx, treatment period. **C** Representative H&E and IHC (H3K27M, H3K27me3, IL-13Rα2, Ki-67, Cleaved Caspase 3, CD68, and NeuN) images of formalin-fixed brain sections from vehicle-, GB13 alone-, RT alone-, and GB13 plus RT-treated PDOX mice euthanized at the ethical endpoint. Images are representative of 4–8 mice in each group. Scale bars: 1×: 1000 μm, 5×: 20 μm, 20×: 20 μm.

Table 2 | Efficacy of combined GB13 and RT in vivo

Animal model	*Treatment condition*			
SU-DIPG XVII PDOX	**CTRL**	**GB13 (5 µg/mL)**	**RT (5 × 2 Gy)**	**GB13 + RT**
Median survival (d)	109	225	170	>350 (alive)
Median survival vs. CTRL (%)	NA	206	156	>320
Median survival vs. CTRL (p-value)	NA	0.0001	0.0614	0.005
Median survival vs. GB13 + RT (p-value)	0.005	0.003	0.006	NA
H3.3 K27M; PDGFRA;p53^{cKO} GEMM	**CTRL**	**GB13 (5 µg/mL)**	**RT (5 × 2 Gy)**	**GB13 + RT**
Median survival (d)	81.5	99.5	91	110
Median survival vs. CTRL (%)	NA	122	117	135
Median survival vs. CTRL (p-value)	NA	0.008	0.1719	≤ 0.0001
Median survival vs. GB13 + RT (p-value)	≤ 0.0001	0.4683	0.0006	NA

Significance of endpoint comparisons between treatment groups were calculated using the Log-rank (Mantel-Cox) test.

in multiple distinct DIPG mouse models. The superior efficacy of combined GB13 and RT compared to using either GB13 or RT alone underscores its potential as a promising radio-immunotherapy approach for this aggressive cancer.

Discussion

DIPG remains one of the most challenging pediatric brain tumors to treat, with RT providing transient improvement of neurological deficits in symptomatic patients[64], reducing steroid utilization[5], and conferring a 3-month survival benefit[16,65,66]. While several treatment modalities have shown promise in preclinical investigations and early-phase clinical studies[67], a plethora of clinical trials with therapeutics have failed to achieve meaningful improvements in survival outcomes[14,15]. Radiosensitization presents a promising avenue for augmenting the efficacy of RT in DIPG, particularly when integrated with emerging treatment strategies. Leveraging the growing body of evidence supporting the effectiveness of IL-13Rα2-targeted immunotherapies[17,68], we sought to investigate the therapeutic potential of combining standard-of-care RT with IL-13Rα2/PE immunotherapy. In previous investigations, cintredekin besudotox (IL13-PE38QQR), a recombinant chimeric cytotoxin composed of wild-type IL-13 and truncated PE, was administered prior to RT for individuals with HGG[36]. The efficacy of cintredekin besudotox was explored in Phase 1–3 clinical trials involving pediatric and adult HGG patients, including those with DIPG[36–39]. Despite showing some promise in these trials, cintredekin besudotox ultimately failed to translate into clinical benefit for a multitude of reasons, including ill-defined trial inclusion criteria, lack of efficacy, and off-tumor toxicity[69–72]. In this context, the IL-13Rα2/PE immunotoxin GB13 was optimized for enhanced tumor cell-selectivity and previously demonstrated robust efficacy in orthotopic xenografts of malignant peripheral nerve sheath tumor[40] and HGG[32] with overexpressed IL-13Rα2 status. In the current study, efficacy of GB13 combined with RT was evaluated in patient-derived DIPG cell cultures and in vivo models, encompassing both immunocompromised PDOX and immunocompetent GEMM, using clinically relevant radiation fractionation schedules. A clear enhancement of radiosensitization coupled with increased tumor cell cytotoxicity was evident in all tested models. These data provide insights to support the clinical advancement of IL-13Rα2-directed radio-immunotherapies for DIPG.

Foundational studies have established IL-13Rα2 as a cancer-specific biomarker, notably overexpressed in a range of malignancies, such as HGG[20], malignant peripheral nerve sheath tumor[40], colorectal cancer[73], ovarian cancer[74], pancreatic cancer[75], and melanoma[76], while largely absent in normal tissues[28]. Subsequent investigations have verified the prevalence of IL-13Rα2 overexpression in a majority of HGG specimens (detected in ~78% of adult glioblastoma [GBM] and 83% of DIPG)[17,25,26,68]. Our computational analyses support these findings, indicating extensive IL-13Rα2 alterations in a spectrum of pediatric brain tumors and revealing a notable co-alteration of IL-13Rα2 and H3-3A in DIPG. Immunohistochemical analysis of brain tissue from deceased patients confirmed the presence of IL-13Rα2 in DIPG, exhibiting minimal intra-tumoral heterogeneity throughout the tumor mass. Additionally, our findings corroborate previous reports of the prognostic significance of IL-13Rα2[20,27]. The critical nature of this is amplified by the observations from our prior investigation, which indicated that the success of IL-13Rα2-targeted immunotherapy is contingent upon tumor IL-13Rα2 expression levels[32]. Hence, IL-13Rα2 is not only a pivotal biomarker but also a prognostic indicator for the selection of patients in clinical trials for IL-13Rα2-directed treatments. In light of these insights, a nuanced appreciation of IL-13Rα2 in DIPG could substantially refine therapeutic approaches and trial designs, paving the way for more individualized and effective treatment modalities for afflicted patients. Critically, information on the specific impact of IL-13Rα2 variants in terms of gain or loss of function, and whether these variants might influence drug response, is currently lacking. The role of IL-13Rα2 variants could be important for understanding differential therapeutic responses, and further studies are necessary to address these questions.

Immunotoxins directed at IL-13 receptors, such as cintredekin besudotox and GB13, harness the IL-13 signaling pathway to selectively deliver cytotoxic payloads to malignant target cells[77]. The targeting moiety of GB13 attaches to IL-13Rα2 at the outer cell membrane of DIPG cells and thereby facilitates internalization of the PE toxin-domain[78]. PE inactivates eukaryotic elongation factor 2 (eEF2) by adenosine diphosphate (ADP)-ribosylation, leveraging oxidized nicotinamide adenine dinucleotide (NAD+) as a substrate[41,42,44]. The inactivation of eEF2 halts protein synthesis and eventually culminates in Bak- and caspase-mediated apoptosis[45,79]. Administration of GB13 resulted in dose-dependent cytotoxicity of treated cells, which was strongly correlated with both the gene expression and protein levels of IL-13Rα2. GB13 exhibited enhanced efficacy relative to cintredekin besudotox, as previously reported in HGG cell lines with elevated IL-13Rα2 expression[28,32,45,80–82]. Furthermore, the IC_{50} of GB13 was up to 3500-fold lower in IL-13Rα2-overexpressing DIPG cell lines compared to non-cancerous brain cells, which lacked detectable IL-13Rα2 protein. These findings suggest that GB13 not only preferentially targets tumor cells with high levels of IL-13Rα2 but also maintains a considerable therapeutic window, indicating its potential as a selective and potent therapeutic option for targeting DIPG via the IL-13Rα2 pathway.

DNA repair is critical for the restoration of damage induced by radiation, and disturbing this repair mechanism can amplify cellular toxicity[60,83]. RT triggers the generation of DNA double-strand breaks (DSBs), which are primarily repaired by the non-homologous end joining machinery (NHEJ)[84]. Consistent with previous investigations involving cintredekin besudotox in GBM cell lines[85], clonogenic survival assays revealed a significant enhancement in the efficacy of RT in DIPG cell lines upon cotreatment with GB13 across multiple radiation doses, with higher concentrations of GB13 resulting in greater sensitization. The LQ model serves as a standard tool for characterizing the dose-response dynamics in

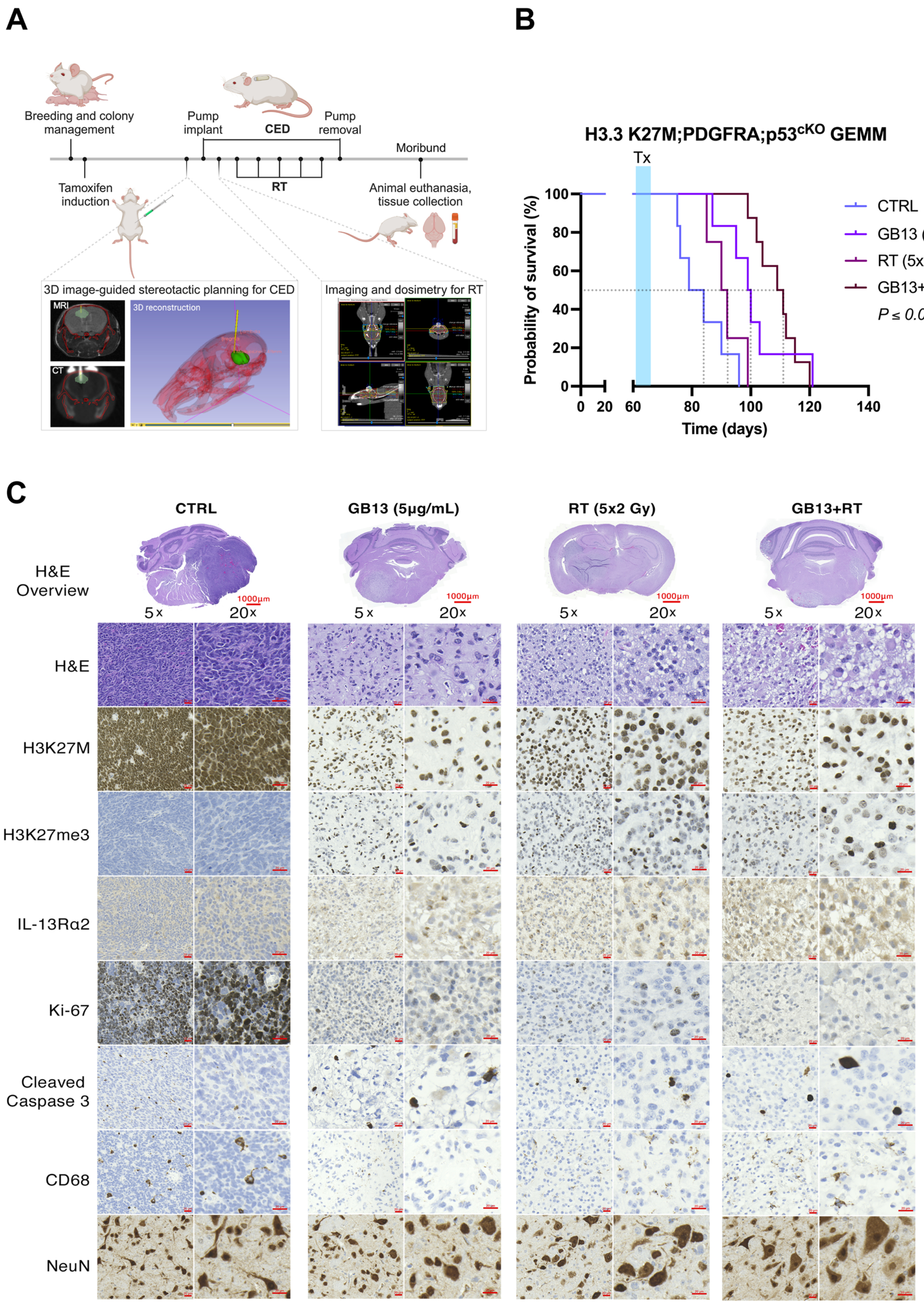

Fig. 6 | GB13 by CED plus concomitant fractionated RT improves the efficacy of either monotherapy alone in a DIPG genetically engineered mouse model (GEMM)[7]. **A** Experimental schema for in vivo efficacy (survival) studies in GEMM animals of mutant *H3F3A*-, *TP53*-, and *PDGFRA*-driven DIPG. Created in BioRender. Rechberger, J. (2025) https://BioRender.com/tcdnc4f. **B** Kaplan–Meier graph for mice (n = 4–8 per group) bearing H3.3 K27M;PDGFRA;p53^{cKO} orthotopic tumors, treated with 7-day continuous CED of GB13 alone (5 μg/mL; purple curve), RT alone (2 Gy once per day for 5 consecutive days; wine-red curve), or the combination of GB13 plus RT (brown curve), compared with vehicle-treated controls (blue curve). $P \leq 0.0001$; Log-rank (Mantel-Cox) test. Tx, treatment period. **C** Representative H&E and IHC (H3K27M, H3K27me3, IL-13Rα2, Ki-67, Cleaved Caspase 3, CD68, and NeuN) images of formalin-fixed brain sections from vehicle-, GB13 alone-, RT alone-, and GB13 plus RT-treated GEMM mice euthanized at the ethical endpoint. Images are representative of 4–8 mice in each group. Scale bars: 1×: 1000 μm, 5×: 20 μm, 20×: 20 μm.

clonogenic survival data derived from RT experiments[86]. The parameters α and β delineate the linear and quadratic components of the curve and offer valuable insights into radiosensitization mechanisms. Radiosensitizing agents have the potential to augment α, β, or both, consequently influencing the α/β ratio, depending on their impact on direct lethal damage, potentially lethal damage (PLD), or sublethal damage (SLD)[87]. With escalating concentrations of GB13 cotreatment at different RT doses, the survival curves did not have a shoulder, with β approaching zero. While estimating β is challenging in this context, the resultant α/β ratio demonstrated a substantial increase. The observed elevation in α upon GB13 cotreatment suggests a likely enhancement of PLD at lower radiation doses[88]. Phosphorylated histone H2AX mediates chromatin response to DSBs in mammalian cells; however, it has minimal effect on overall NHEJ efficiency. Cotreatment with GB13 markedly elevated levels of γH2AX in DIPG cells following radiation, indicating that it potentiated the DNA damage response induced by RT. These findings consistently support a radiosensitizing effect of GB13 attributed to the inhibition of DNA repair capacity. The synergistic effects of GB13 and RT are further supported by their combined impact on apoptosis induction, as evidenced by the decrease in Mcl-1 and increased cleaved caspase 3 and cleaved PARP-1 levels[89,90].

Combining neoadjuvant and concomitant administration of GB13 with RT offers several advantages over existing therapeutic strategies for DIPG[6,91]. This dual approach harnesses the specificity of targeted immunotherapy while capitalizing on the cytotoxic effects of RT to exert a synergistic effect against tumor cells. In a PDOX model that closely recapitulates the molecular characteristics of human DIPG tumors[92], mice subjected to combined GB13 and RT treatment showed significantly prolonged survival compared to monotherapy or control groups. Importantly, these findings were corroborated in an immunocompetent GEMM[63], where immunotoxin therapy and RT did not induce a significant increase in immune cell infiltration or inflammatory responses[93]. Moreover, our in vivo studies demonstrate the tolerability of combined CED of GB13 and RT. Coadministration of GB13 with fractionated focal irradiation (5 × 2 Gy, 10 Gy in total) delivered to the pons did not result in overt neurological defects or histopathological alterations in brains of mice post-treatment. Surprisingly, effects of GB13 and/or combination with RT were sustained, as observed by Ki-67 and caspase cleavage signaling detection in tumors at time of animal sacrifice. Reduction of Ki-67 is reflective of an anti-tumor response, relative to control treatment, which resulted in increased animal survival. This is consistent with previous studies demonstrating that increased animal survival correlated with decreased tumor growth rate. The prolonged caspase 3 cleavage signal was reproducible in all CED model studies and unexpected. This persistent signal warrants further investigation to determine if the tumor microenvironment induced by pro-apoptotic treatments, including GB13, elicits an immunogenic bystander response. Together, the use of a clinically relevant dosing regimen and locoregional drug delivery system to circumvent the BBB enhances the translational potential of our findings, providing a strong rationale for further investigation of this novel radio-immunotherapy approach[94].

There are several limitations to our study. First, our findings are based on preclinical models and may not fully recapitulate the complexity of human DIPG. While our in vitro and in vivo models recapitulate some of the key features of DIPG, the translation of these findings to clinical settings may face challenges related to tumor heterogeneity and patient-specific factors[95,96]. With this respect, it remains questionable how effective the proposed treatment regimen can be if IL-13Rα2 is heterogeneously expressed, as both animal models used in this study uniformly overexpressed IL-13Rα2. Second, further optimization of the treatment protocol, including assessment of long-term toxicity, is needed to determine the optimal therapeutic regimen for GB13-RT combination therapy[97]. Additionally, the potential development of resistance mechanisms to GB13[78] and the impact of tumor microenvironment factors[98–100] on treatment response require further investigation.

In conclusion, we report that radiotherapy plus neoadjuvant and concomitant GB13 can be used to effectively treat in vitro and in vivo models of DIPG. We demonstrated the radiosensitizing properties of GB13 in a panel of patient-derived DIPG cell lines, mediated by inhibition of DNA damage repair and convergent modulation of apoptotic signaling pathways. Treatment of DIPG-bearing mice with combined GB13 and RT resulted in significant survival prolongation and durable pharmacodynamic effects compared to individual treatment modalities alone. Together, our results provide a strong rationale for further exploration of this innovative radio-immunotherapy strategy through rigorous preclinical and clinical investigations.

Methods

Human IL-13Rα2 expression

The cBioPortal for Cancer Genomics (http://cbioportal.org) and the Open Pediatric Brain Tumor Atlas (OpenPBTA) dataset in PedcBioPortal (https://pedcbioportal.org) were accessed and analyzed to evaluate IL-13Rα2 RNA expression across pediatric brain tumors using RNA-Seq and patient clinical information[48–51]. Comparisons of IL-13Rα2 expression were performed based on pediatric brain cancer types with respect to total RNA and incidence of increased expression, H3-3A status, and overall survival. Specifically, for Fig. 1A, the y-axis represents $\log2(x + 1)$ transformed RSEM normalized counts, a standard transformation used to normalize and stabilize the variance of gene expression data and facilitate downstream comparisons. A log2 fold change was utilized to report gene expression levels on a logarithmic scale (base 2), where a log2 fold change of 1.5 indicates a multiplicative factor increase in gene expression of $2^{1.5}$ (about 2.82). For normalization, the normalize Quantiles method was applied to the $\log2(x + 1)$ transformed RSEM normalized counts, which ensures a uniform distribution across samples and mitigates technical variation[51,101]. For protein or peptide abundance, the median log2 relative abundance was calculated for each sample and normalized to a common median of 0.

To confirm the presence of IL-13Rα2 protein in DIPG patients, samples of tumor tissue (brainstem) and matched normal brain tissue (uninvolved frontal cortex or adjacent brainstem) were acquired through autopsy. Informed consent in compliance with institutional review board (IRB) approval at Mayo Clinic was obtained for all human tissue studies. The cohort included 2 males with radiographically and clinically diagnosed DIPG, aged 9 and 11 yrs at the time of diagnosis. Both patients passed away within the first year after their diagnoses. Tumor and brain samples were harvested during the autopsy and preserved using formalin fixation and paraffin embedding (FFPE). Tissue sections were then subjected to hematoxylin and eosin (H&E) as well as immunohistochemistry (IHC) staining as detailed below.

Cell lines and culture

All research involving patient tumor-derived DIPG cell lines received informed consent and approval from the Mayo Clinic IRB. Early-passage DIPG cell lines that were established from biopsy or autopsy material obtained from DIPG patient cases were used, and the authenticity of cell lines was confirmed annually by short tandem repeat (STR) DNA fingerprinting. Normal human astrocytes (NHA; primary brain cells derived from human embryos) were purchased from Lonza Bioscience (Walkersville, MD, USA) and handled in accordance with the manufacturer's recommendations. All cell lines were checked for Mycoplasma contamination every 3 months. Sanger sequencing for detection of histone H3 gene mutations in cell lines with the H3K27M mutation was performed over the same interval. The primer sequences used for Sanger sequencing were: H3-3A K27M (forward sequence: 5′-GTT TGG TAG TTG CAT ATG GTG ATT-3′; reverse sequence: 5′-ACA AGA GAG ACT TTG TCC CAT T-3′) and H3C2 K27M (forward sequence: 5′-GGG CAG GAG CCT CTC TTA AT-3′; reverse sequence: 5′-ACC AAG TAG GCC TCA CAA GC-3′). DIPG cells were periodically validated for H3K27M-mutant histone expression and loss of H3K27me3 by Western blotting as previously described[102]. Neurosphere-cultured cells were passaged every 1–2 weeks, while cells cultured as adherent monolayers were passaged 1–2 times per week. Details regarding cell line origin, molecular status, culture medium, and other pertinent information for each cell line are listed in Supplementary Tables 1 and 2.

Drugs and radiation for in vitro experiments

GB13 (IL13.E13K-PE4E) was generously provided by Targepeutics, Inc. (Hershey, PA, USA). The drug was dissolved in PBS and stored as a 2.6 mg/mL stock solution at −80 °C. For in vitro experiments, GB13 was diluted in Dulbecco's Phosphate-Buffered Saline (DPBS; Cat #14190-144; Thermo Fisher Scientific, Waltham, MA, USA) and then added to cells in the appropriate cell culture medium at the desired concentration. All cell irradiation treatments were performed using a X-RAD 320 irradiator (Precision XRay, Inc., North Branford, CT, USA), which generates orthovoltage X-rays. The dimensions and positions of various components including the source, the aluminum filter, and the collimator within the X-RAD 320 irradiator were set to expose cells to specified doses of radiation at a dose rate of ~3 Gy/min (225 kVp, 17.7 mA, 2 mm Al filter, 50 cm distance from source)[103].

Proliferation and viability assay

Cells in single-cell suspension were plated in the appropriate cell culture medium in 96-well clear-bottom black microplates (Cat #3917; Corning Costar, Corning, NY, USA) at a density of 5,000 cells per well (SU-DIPG IV, SU-DIPG XIII, SU-DIPG XVII, SF8628, and NHA[104,105]). Cells were cultured overnight at 37 °C with 5% CO_2. The next day, cells were treated in triplicate with either vehicle (DPBS) or serial dilutions of GB13 (to final concentrations of 320, 100, 32, 10, 3.2, 1, 0.32, 0.1, 0.032, 0.01, 0.0032, and 0.001 ng/mL). Cells were subsequently incubated for 72 h and then assayed with CellTiter-Glo Luminescent Cell Viability Assay (Cat #G7570; Promega, Madison, WI, USA) according to manufacturer recommendations. Luminescence was measured using an Infinite M200 PRO multimode microplate reader (Tecan Group, Männedorf, Switzerland), normalized to control wells, and relative luminescence treatment was plotted as a function of drug concentration. The potency (half-maximal inhibitory concentration, IC_{50}) of each treatment was calculated by non-linear least-squares curve fitting using Prism 10 (GraphPad, San Diego, CA, USA). The therapeutic index of GB13 for high-grade glioma (HGG) cell lines was calculated as the ratio of the dose that induces toxicity to the dose that produces a clinically desired or effective response. In this study, the calculation of the therapeutic index was based on the comparison of the IC_{50} values in NHA and individual tumor cell lines.

The formula used for calculating the therapeutic index is expressed as follows:

$$\text{Therapeutic index} = \frac{\text{IC50 in NHA}}{\text{IC50 inindividual tumor cell line}}$$

Where:

- IC_{50} in NHA represents the half-maximal inhibitory concentration of GB13 in primary cells of the central nervous system (CNS).
- IC_{50} in individual tumor cell line represents the half-maximal inhibitory concentration of GB13 in the specific HGG cell line under consideration.

A higher therapeutic index value indicates a greater selectivity of GB13 for tumor cells over normal cells, suggesting a more favorable therapeutic profile. The calculation of therapeutic index serves as an important parameter in assessing the potential clinical applicability and safety profile of GB13 for HGG treatment[106].

RNA-sequencing

A RNeasy Plus micro kit (Cat #74034; QIAGEN, Germantown, MD, USA) was used per the manufacturer's instructions to extract total RNA from whole-cell lysates. RNA-Seq experiments were conducted as single replicates for the purpose of screening a large library of cell lines. RNA quality control, library preparation, and sequencing were performed by Novogene (Beijing, China). The integrity, purity, and quantification of RNA samples was verified using a NanoPhotometer spectrophotometer (IMPLEN, Westlake Village, CA, USA), 1% agarose gel electrophoresis, and Bioanalyzer 2100 (Agilent Technologies, Santa Clara, CA, USA). RNA sample preparation was performed using 1 μg of RNA per sample, and the NEBNext UltraTM RNA Library Prep Kit for Illumina sequencers (New England Biolabs, Ipswich, MA, USA) was used for library preparation. Subsequently, cDNA fragments of 150–200 bp in length were selected using AMPure XP magnetic beads (Beckman Coulter, Pasadena, CA, USA). Final library quality was validated with a Bioanalyzer 2100 (Agilent Technologies). A NovaSeq 6000 sequencer (Illumina, San Diego, CA, USA) was used to perform clustering of index-coded samples per manufacturer instructions. Sample libraries were sequenced using either single- or paired-end sequencing, depending on the timeframe of sample availability and the sequencing technology available. Paired-end sequencing data on adult GBM cell lines were obtained from cBioPortal, a freely accessible online platform that provides RNA-Seq data on Mayo Clinic's brain tumor patient-derived xenografts[48,49]. Quality control of generated FASTQ files was performed using FASTQC, and reads were trimmed using a FASTX trimmer (http://hannonlab.cshl.edu/fastx_toolkit/). The trimmed reads were aligned to the hg38 reference genome using STARv2.7.3a, and the gene counts were derived by annotating the aligned reads using the –quantMode geneCounts function[107]. Finally, transcripts per million (TPM) or reads per kilobase per million (RPKM) values were computed using RSEM, following the library's single- or paired-end status[108].

Western blot

Cells were plated in single-cell suspensions in T25 flasks (Cat # 430639; Corning) at a seeding density of 1 × 10^6 cells per flask and cultured for 24 h at 37 °C with 5% CO_2. Cells that were treated with monotherapy received GB13 at concentrations equal to the IC_{50} established by CellTiter-Glo Luminescent Cell Viability Assay (Promega) or were subjected to radiation using an X-RAD 320 irradiator (Precision XRay, Inc.). The cells were then trypsinized and collected between 1 h to 72 h after the start of treatment. Cells receiving combination therapy were pretreated with GB13 at an IC_{50} concentration 1 h to 24 h before radiation, and they were trypsinized and collected between 1 h to 48 h after radiation. Collected cell pellets were centrifuged twice at 500 × *g* for 3 min, with the supernatant being removed and the pellets being resuspended in DPBS. Cells were then lysed in Triton X-100 lysis buffer containing protease inhibitors and sonicated using an ultrasonic processor (Cat #Z528897; Sigma-Aldrich, St. Louis, MO, USA). All protein lysates were stored at −20 °C until further use. Protein was quantified using a Pierce BCA Protein Assay Kit (Cat #23227; Thermo Fisher Scientific). Then, 15 μg of total protein per sample was size fractioned by 12.5% SDS-PAGE. After electrophoresis, proteins were electrically transferred to a polyvinylidene difluoride (PVDF) membrane, rinsed in PBST buffer, blocked in 2% fat-free milk for 1 h at room temperature, and incubated with primary antibody overnight at 4 °C. After primary antibody blotting, a species-specific peroxidase-conjugated secondary antibody (Thermo Fisher Scientific) was used to detect the specific signal. This was achieved by using SuperSignal West Pico PLUS Chemiluminescent Substrate (Cat #34580; Thermo Fisher Scientific) and capturing images with an Azure 600 Western blot imaging system (Azure Biosystems, Dublin, CA, USA). Details regarding antibodies used for Western blot can be found in Supplementary Table 3.

Clonogenic assay

Appropriate numbers of cells were counted, placed in single-cell suspension, plated in 6-well flat-bottom clear plates (Cat # 353046; Corning), and cultured overnight at 37 °C with 5% CO_2. The following day, cells were treated with various concentrations of GB13 or vehicle (DPBS) for a total of 72 h. An irradiation dosage of 0 to 10 Gy was administered to cells 24 h after the start of drug treatment. At the end of the treatment period, cells were rinsed with PBS and incubated in fresh media for 7-10 d to allow for colony formation. Subsequently, cells were again rinsed with PBS, stained with

Coomassie Brilliant Blue G-250 (Cat # 20279; Thermo Fisher Scientific) for 60 min, washed with deionized water (ddH$_2$O), and left to dry at room temperature for 24 h. Colonies were then quantified and analyses performed as detailed below.

For synergy analyses, Zero Interaction Potency (ZIP)[57], Loewe additivity[55], Highest Single Agent (HSA)[56], and Bliss[54] reference models were used to calculate synergy score statistics. SynergyFinder was used for interactive analysis and visualization of treatment combination profiling data[52,53]. The summary of synergy scores were evaluated as follows: Less than −10: the interaction between two treatments is likely to be antagonistic; From −10 to 10: the interaction between two treatments is likely to be additive; Larger than 10: the interaction between two treatments is likely to be synergistic[109,110].

γH2AX immunofluorescence assay

Cells in single-cell suspension were plated on chambered culture slides (Cat #229164; CELLTREAT Scientific Products, Pepperell, MA, USA) with a seeding density of 10,000 cells per well and cultured for 24 h at 37 °C with 5% CO$_2$. Cells undergoing monotherapy were subjected to GB13 at concentrations equivalent to the IC$_{50}$ determined by CellTiter-Glo Luminescent Cell Viability Assay (Promega), or were exposed to radiation using an X-RAD 320 irradiator (Precision XRay, Inc.). Subsequently, cells were washed with PBS and then fixed with 4% paraformaldehyde for 20 min at room temperature, either 1 h, 4 h, or 24 h after the start of treatment. Cells receiving combination therapy were pretreated with IC$_{50}$ concentrations of GB13 24 h prior to radiation, and rinsed and fixed either 1 h, 4 h, or 24 h after irradiation. Cells were then washed with PBS 2 times for 5 min and permeabilized with 0.5% Triton X-100 for 5 m. Permeabilization buffer was washed of cells with PBS 3 times for 5 min, and cells were blocked with 3% BSA in PBST for 1 h at room temperature. After this, cells were incubated with γH2AX antibody (listed in Supplementary Table 3) in 1% BSA in PBST at 4 °C overnight. The following day, cells were washed of primary antibody with PBST 3 times for 5 min and incubated with Alexa Fluor-coupled secondary antibody (Thermo Fisher Scientific) for 1 h at room temperature. Cells were then washed with PBS 3 times for 5 min and counterstained with DAPI in PBS for 90 s. Finally, cells were washed with PBS 3 times for 5 min, rinsed with ddH$_2$O, and mounted using SlowFadeTM Glass Antifade Mountant (Cat #S36917; Thermo Fisher Scientific). A LSM980 confocal laser scanning microscope (Carl Zeiss Microscopy, White Plains, NY, USA) was utilized to capture 12 images per well utilizing an automated grid at a magnification of 20X. Cells were counted using a custom-built ImagePro (Version 10; Media Cybernetics, Rockville, MD, USA) macro based on the DAPI staining. Only images containing more than 5 cells were analyzed. The number of γH2AX foci was determined by utilizing the "Find maxima" feature in ImageJ, with a prominence threshold set at 35. Three biological replicates with at least 2 technical replicates were performed for all conditions. At least 700 cells were analyzed per condition. Data were exported and analyzed using Prism 10 (GraphPad) and presented as mean foci per cell.

Animal models

Approval for animal experiments. All animal experiments were conducted in accordance with National Institutes of Health (NIH) and Institutional Animal Care and Use Committee (IACUC) guidelines for the use of animals in research and approved by the Mayo Clinic Institutional Committee for Animal Research. Authors complied with the Animal Research: Reporting of In Vivo Experiments (ARRIVE) guidelines (https://arriveguidelines.org/).

SU-DIPG XVII patient-derived orthotopic xenograft (PDOX). Orthotopic tumor inoculation of patient-derived DIPG cells was performed as previously described[32,62,102]. Briefly, SU-DIPG XVII cells were tagged by transduction with a pRRLSIN-18.PPT. LUC-GFP.pre lentiviral vector (generously provided by Dr. Michelle Monje, Stanford University)[92,111]. Transduced cells were enriched based on stable integration and authenticated. Xenografts were created by injecting 500,000 cells placed in single-cell suspension in 5 µL of sterile DPBS (Thermo Fisher Scientific) into the pons of 6–7 week-old female athymic nude mice (Hsd:Athymic Nude-Foxn1^{nu}/Foxn1^{nu}; Charles River Laboratories, Wilmington, MA, USA). Mice were anesthetized with 100 mg/kg of ketamine and 10 mg/kg of xylazine and placed in a stereotactic frame (Model 502650; World Precision Instruments, Sarasota, FL, USA). Using stereotactic technique, a 0.5 mm burr hole was created with a MH-130 portable drill (Foredom, Bethel, CT, USA) at the following coordinates: 2 mm lateral and 1 mm caudal to the lambda. Tumor cells were administered with a 26 gauge (51 mm, point style AS) syringe (Cat #203185; Hamilton Company, Bonaduz, Switzerland) at a steady rate of 0.5 µL/min using a Quintessential Stereotaxic Injector (QSI™; Stoelting, Wood Dale, IL, USA). To reach the ventrolateral pons, the needle was inserted to a depth of 4.2 mm[112]. Following the injection, the burr hole was sealed with bone wax (Corza Medical, Westwood, MA, USA), and the skin was closed using wound clips (Fine Science Tools, Foster City, CA, USA). In vivo tumor engraftment and progression was monitored by bioluminescence imaging (BLI). Animals were dosed with an intraperitoneal injection of luciferase substrate (10 mg/kg CycLuc1; Glixx Laboratories, Hopkinton, MA, USA). Following a 10-min period, mice were subjected to imaging while under 2% isoflurane anesthesia utilizing an IVIS-200 Imaging System (Xenogen Corporation, Berkeley, CA, USA). Image analysis was conducted using LivingImage 4.3 (PerkinElmer, Waltham, MA, USA) to quantitate the total flux (photons/sec) within the region of interest.

H3.3 K27M; PDGFRA; p53^{cKO} genetically-engineered mouse model (GEMM). A spontaneous brainstem glioma mouse model with H3-3A-, TP53-, and PDGFRA mutations was created in Dr. Suzanne Baker's (St. Jude Children's Research Hospital) laboratory and kindly gifted to us for this study[63]. Genetically-engineered mice harboring H3f3a$^{LSL\text{-}K27M\text{-}Tag/+}$,Trp53^{flox}, or LSL-PDGFRA^{V544ins} were bred to tamoxifen-inducible Nestin-CreER^{T2} mice. After induction with tamoxifen at P0 and P1, triple-transgenic (H3.3 K27M; PDGFRA; p53^{cKO}) mice developed spontaneous and highly penetrant high-grade brainstem gliomas from postnatal neural progenitors that resemble human DIPG. The distribution was approximately equal between male (n = 20; 54%) and female (n = 17; 46%) mice. Autochthonous tumor development was tracked by MRI using a Bruker Avance 300 MHz (7 Tesla) vertical bore nuclear MR spectrometer (Bruker Biospin, Billerica, MA, USA). Mice were anesthetized with 2% isoflurane and placed in the MRI scanner outfitted with a constant isoflurane inhalation system. Three-dimensional (3D) T2-weighted fast spin echo sequences were acquired with echo time (TE)/repetition time (TR) = 45.20/2000 ms, bandwidth (BW) = 110 kHz. The total imaging time per mouse was ~10 min per scan. Animal core body temperatures were regulated at 37 °C with the use of a warm air flow.

Drugs and radiation for in vivo experiments. As mentioned above, the IL-13Rα2 immunotoxin GB13 was obtained from Targepeutics, Inc. GB13 was dissolved in PBS and maintained at a temperature of −80 °C as a stock solution with a concentration of 2.6 mg/mL. For in vivo experiments, GB13 was diluted to the required concentrations for CED in DPBS (Thermo Fisher Scientific). Radiation was delivered to anesthetized mice using a 15 mm rectangular collimator with opposing lateral beams (225 kVp, 20 mA, 0.3 mm Cu filter) delivered with a PXI X-RAD SmART + irradiator (Precision XRay)[61]. A total of 2 Gy of radiation was given to each mouse per session, which consisted of a 0.9 Gy dose to isocenter with a beam duration of 15 s from each opposing lateral beam.

CED. For brain-targeted drug delivery, mice were randomized to vehicle control (PBS) and treatment (GB13) groups based on BLI (PDOX) or MRI (GEMM) signal to ensure a uniform distribution of tumor size at the beginning of the study. A BLI signal of 200,000 total log flux was used as the tumor size threshold to start treating PDOX animals. Therapy for GEMM animals was initiated on postnatal day 70 and was randomized according to tumor volumetric analyses, as previously described[62].

Prior to starting GB13 treatment, osmotic drug infusion pumps for accurate and continuous dosing of unrestrained mice (ALZET Model 2001; infusion rate: 1 µL/h; DURECT Corporation, Cupertino, CA, USA) were primed per the manufacturer's instructions. Each pump received a designated amount of GB13 stock solution dissolved in sterile DPBS (Thermo Fisher Scientific) to attain the following final drug concentrations: 0 µg/mL (vehicle control), 1.5 µg/mL, 5 µg/mL, and 15 µg/mL. Pumps were attached to a vinyl catheter primed with the drug solution and connected to a 30 gauge infusion cannula (Cat # 8IC315IS5SPC; 5 mm projection below the pedestal; P1 Technologies, Roanoke, VA, USA).

To implant the drug infusion pumps, mice were placed under anesthesia with a constant inhalation flow of 2% isoflurane. A 2 cm midline skin incision was made, starting at the posterior aspect of the eyes and extending to the level of the ears, in order to expose the skull. Using a MH-130 portable drill (Foredom), a 0.5 mm burr hole was created: For PDOX mice, the existing burr hole used for tumor cell inoculation was reopened. The coordinates identified by MRI were used for targeting each GEMM tumor. Next, a hemostat (Fine Science Tools) was used to create a subcutaneous pocket between the scapulae at the posterior end of the skin incision. The infusion pump connected to the infusion cannula via a vinyl catheter was subsequently introduced into the subcutaneous pocket. Dental glue primer (Kulzer North America, South Bend, IN, USA) was applied to the skull surrounding the burr hole using a 0.3 mL insulin syringe (Becton, Dickinson and Company, Franklin Lakes, NJ, USA), and the primer was activated with UV light. Then, mice were placed on a stereotactic stage (World Precision Instruments) with automated thermal support using a Rodent Warmer X1 (Cat #53800 M; Stoelting), and a stereotactic arm was used to insert the infusion cannula (P1 Technologies). Dental glue (Ivoclar Vivadent, Schaan, Liechtenstein) was used to affix the infusion cannula to the skull. Finally, the skin incision was closed with wound clips (Fine Science Tools).

All mice were closely monitored throughout the CED infusion and had their infusion pumps removed 7 days after they were implanted. For this procedure, animals were anesthetized with 2% isoflurane and a small skin incision was made between the scapulae near the rostral end of the pump. The catheter was disconnected and sealed with bone wax (Corza Medical), and the pump was removed while leaving the infusion cannula in place. The incision was closed using wound clips (Fine Science Tools).

RT. Twenty-four hours after the commencement of CED of GB13, mice were subjected to a CT scan for dosimetry using a PXI X-RAD SmART+ irradiator (Precision XRay) and the dedicated small animal radiotherapy planning system SmART-ATP (SmART Scientific Solutions B.V., Maastricht, The Netherlands)[113]. For each beam direction, a two-dimensional area was defined based on the projection of the target volume in the pons. The radiation field covered the hindbrain, midbrain, and most of the forebrain, with additional coverage of the base of skull bones and the upper cervical spine. Oral cavity and olfactory bulbs were protected from radiation exposure to the greatest extent feasible. The following day, mice were placed under anesthesia with a constant inhalation flow of 2% isoflurane and dosed with 2 Gy of radiation to the predefined target volume. The time for radiation delivery per mouse was 30 s (15 s from each opposing lateral beam). Animal core body temperatures were regulated at 37 °C with the use of a warm air flow in the radiation chamber. This procedure was repeated every 24 h until each mouse received a total radiation dose of 5 × 2 Gy.

Outcomes. Following cessation of treatment, animals were monitored daily and euthanized by CO_2 inhalation at indication of progressive neurological deficit or if found in a moribund condition. More specifically, IACUC endpoint guidelines for euthanasia included weight loss ≥20%, inability to reach food/water, immobility, hunched posture, lethargy, spasticity, seizures, circling, and paralysis. Brains were harvested immediately after euthanasia and fixed in 4% paraformaldehyde at room temperature overnight. On the subsequent day, brains were transferred to a 4 °C fridge and stored until further use. The number of days that mice survived after orthotopic tumor inoculation or tamoxifen induction was documented for the purpose of conducting Kaplan-Meier analyses in PDOX and GEMM studies, respectively.

Immunohistochemistry

Formalin-fixed tissue specimens were embedded in paraffin and sectioned in the coronal plane (5 µm/section) using a microtome (CM1860 UV; Leica Biosystems, Buffalo Grove, IL, USA). H&E staining was conducted according to standard protocol[114]. IHC staining was performed in collaboration with the Pathology Research Core at Mayo Clinic using the BOND RX Stainer (Leica Biosystems). Briefly, tissue sections were dewaxed in xylene and rehydrated in ethanol. Antigen retrieval was performed by steaming slides in preheated sodium citrate buffer (10 mM tri-sodium citrate, 0.05% Tween 20, pH 6.0) for 30 min. Slides were then cooled to room temperature and rinsed with ddH_2O for 1 min. Next, slides were immersed in a solution of 0.6% hydrogen peroxide (H_2O_2) in methanol (CH_3OH) for a duration of 20 min. This was followed by blocking slides with 10% normal goat serum (NGS) in Tris-buffered saline (TBS) for 30 min at room temperature. Primary antibodies were diluted in TBS containing 2% NGS and 0.5% Triton X-100 and applied to slides overnight at 4 °C. On the following day, slides underwent three rounds of washing for a duration of 5 min each in TBS containing 2% NGS and 0.5% Triton X-100. The VECTASTAIN Elite ABC kit (Cat # PK-6100; VECTOR Laboratory, Burlingame, CA, USA) containing biotinylated secondary antibody was diluted in TBS with 1.5% NGS and applied to slides according to the manufacturer's instructions. Following three additional 5-min washes in TBS, slides were incubated with Avidin/Biotinylated Enzyme Complex (ABC) solution (Cat #PK-6100; VECTOR Laboratory) for 30 min at room temperature. Slides were subsequently developed with SignalStain DAB Substrate Kit (Cat #8059 P; Cell Signaling, Danvers, MA, USA). Finally, slides were counterstained with hematoxylin and mounted with PermountTM (Cat #SP15-100, Thermo Fisher Scientific). Images were acquired using a digital slide scanner equipped with a 20× objective lens (Axio Scan.Z1; Carl Zeiss Microscopy). Cellular quantification was conducted using the Cell Counter plugin of ImageJ software (NIH). For each antibody, images from 3 randomly selected high-power fields were captured, encompassing up to 300 cells per field. The data are expressed as the percentage of positively stained cells relative to the total number of cells counted. Additionally, low-magnification images are provided to confirm the uniformity of the staining across the tissue sections. Detailed information regarding antibodies used for immunohistochemistry is provided in Supplementary Table 3.

Statistical analyses

Data are presented as mean ± standard deviation (SD) or mean ± standard error of the mean (SEM) as applicable. Student's t test, one-way or two-way analysis of variance (ANOVA) followed by the Tukey or Dunnett's post hoc test were applied for comparison between two groups or among multiple groups, respectively. Non-linear least-squares curve fitting was used to determine the IC_{50} of GB13 in cultured cells and the in vitro correlation between IL-13Rα2 gene expression and GB13 sensitivity. Survival fractions (SF) in clonogenic assays represent normalized plating efficiency or % neurosphere count relative to controls. Survival curves were fitted to a linear quadratic (LQ) cell death model. SF was related to radiation dose (D) by $SF = e^{-(\alpha D+\beta D^{\wedge}2)}$, where α and β are experimentally derived parameters. Sensitizer Enhancement Ratio at 10% survival (SER10) was calculated as fold change in D at survival fraction 0.1 (or 10%) by addition of GB13, where D for each condition was extrapolated by solving the equation $0.1 = e^{-(\alpha D+\beta D^{\wedge}2)}$. ELDA webtool (http://bioinf.wehi.edu.au/software/elda/) was used to evaluate differences in clonogenic cell frequencies across treatment groups[115], and the colony area percentage and colony intensity percentage were calculated using ColonyArea tool[58]. Each in vitro experiment was repeated at least three times independently with similar results, and the representative data is presented. Mouse survival data was analyzed using the Kaplan-Meier estimate with Log-Rank (Mantel-Cox) test. Pairwise comparisons between individual treatment groups were conducted using the Bonferroni correction to account for multiple comparisons and control for the increased risk of Type I error. Survival data was reused across multiple experiments where appropriate. All statistical tests and analyses were conducted using Prism 10 (GraphPad), with statistical significance set at an α threshold of 0.05 and $p < 0.05$.

Reporting summary

Further information on research design is available in the Nature Portfolio Reporting Summary linked to this article.

Data availability

The data that support the findings of this study are available within the paper and its Supplementary Information. RNA-Seq data has been uploaded to GEO under accession number GSE288070. Compiled blot/gel images are included in Supplementary Fig. 8. High-resulution and uncropped IHC images as well as uncropped and unedited images of Western blots are also included in the Supplementary Material file. Additional data are available from the corresponding author upon reasonable request.

Received: 31 August 2024; Accepted: 30 October 2025;

References

1. Ostrom, Q. T. et al. CBTRUS statistical report: pediatric brain tumor foundation childhood and adolescent primary brain and other central nervous system tumors diagnosed in the United States in 2014-2018. *Neuro Oncol.* **24**, iii1–iii38 (2022).
2. Siegel, R. L., Miller, K. D., Wagle, N. S. & Jemal, A. Cancer statistics, 2023. *CA Cancer J. Clin.* **73**, 17–48 (2023).
3. Siegel, D. A. et al. Counts, incidence rates, and trends of pediatric cancer in the United States, 2003-2019. *J. Natl. Cancer Inst.* **115**, 1337–1354 (2023).
4. Ostrom, Q. T., Cioffi, G., Waite, K., Kruchko, C. & Barnholtz-Sloan, J. S. CBTRUS statistical report: primary brain and other central nervous system tumors diagnosed in the United States in 2014-2018. *Neuro Oncol.* **23**, iii1–iii105 (2021).
5. Hargrave, D., Bartels, U. & Bouffet, E. Diffuse brainstem glioma in children: critical review of clinical trials. *Lancet Oncol.* **7**, 241–248 (2006).
6. Warren, K. E. Diffuse intrinsic pontine glioma: poised for progress. *Front. Oncol.* **2**, 205 (2012).
7. Gupta, N. et al. Prospective feasibility and safety assessment of surgical biopsy for patients with newly diagnosed diffuse intrinsic pontine glioma. *Neuro Oncol.* **20**, 1547–1555 (2018).
8. Rechberger, J. S. et al. Feasibility of probe washing after stereotactic needle biopsy as a novel technique for developing cell lines and xenografts of H3 K27-altered diffuse midline gliomas. *J. Neurosurg. Pediatr.* **32**, 413–420 (2023).
9. Dalmage, M. et al. Survival and neurological outcomes after stereotactic biopsy of diffuse intrinsic pontine glioma: a systematic review. *J. Neurosurg. Pediatr.* **32**, 665–672 (2023).
10. Cooney, T. et al. Contemporary survival endpoints: an International Diffuse Intrinsic Pontine Glioma Registry study. *Neuro Oncol.* **19**, 1279–1280 (2017).
11. Saratsis, A. M., Knowles, T., Petrovic, A. & Nazarian, J. H3K27M Mutant Glioma: disease definition and biological underpinnings. *Neuro Oncol*. https://doi.org/10.1093/neuonc/noad164 (2023).
12. Giagnacovo, M. et al. Retrospective analysis on the consistency of MRI features with histological and molecular markers in diffuse intrinsic pontine glioma (DIPG). *Childs Nerv. Syst.* **36**, 697–704 (2020).
13. Tam, L. T. et al. MRI-based radiomics for prognosis of pediatric diffuse intrinsic pontine glioma: an international study. *Neurooncol. Adv.* **3**, vdab042 (2021).
14. Rechberger, J. S., Lu, V. M., Zhang, L., Power, E. A. & Daniels, D. J. Clinical trials for diffuse intrinsic pontine glioma: the current state of affairs. *Childs Nerv. Syst.* **36**, 39–46 (2020).
15. Dalle Ore, C., Coleman, C., Gupta, N. & Mueller, S. Advances and clinical trials update in the treatment of diffuse intrinsic pontine gliomas. *Pediatr. Neurosurg.* **58**, 259–266 (2023).
16. Kim, H. J. & Suh, C. O. Radiotherapy for diffuse intrinsic pontine glioma: insufficient but indispensable. *Brain Tumor Res. Treat.* **11**, 79–85 (2023).
17. Berlow, N. E. et al. IL-13 receptors as possible therapeutic targets in diffuse intrinsic pontine glioma. *PLoS ONE* **13**, e0193565 (2018).
18. Joshi, B. H., Plautz, G. E. & Puri, R. K. Interleukin-13 receptor alpha chain: a novel tumor-associated transmembrane protein in primary explants of human malignant gliomas. *Cancer Res.* **60**, 1168–1172 (2000).
19. Rahaman, S. O. et al. IL-13R(alpha)2, a decoy receptor for IL-13 acts as an inhibitor of IL-4-dependent signal transduction in glioblastoma cells. *Cancer Res.* **62**, 1103–1109 (2002).
20. Zeng, J. et al. IL13RA2 is overexpressed in malignant gliomas and related to clinical outcome of patients. *Am. J. Transl. Res.* **12**, 4702–4714 (2020).
21. Lupardus, P. J., Birnbaum, M. E. & Garcia, K. C. Molecular basis for shared cytokine recognition revealed in the structure of an unusually high affinity complex between IL-13 and IL-13Ralpha2. *Structure* **18**, 332–342 (2010).
22. Cheng, Y. et al. Blood-brain barrier permeable gold nanoparticles: an efficient delivery platform for enhanced malignant glioma therapy and imaging. *Small* **10**, 5137–5150 (2014).
23. Tu, M. et al. IL-13 receptor α2 stimulates human glioma cell growth and metastasis through the Src/PI3K/Akt/mTOR signaling pathway. *Tumour Biol.* **37**, 14701–14709 (2016).
24. Bhardwaj, R., Suzuki, A., Leland, P., Joshi, B. H. & Puri, R. K. Identification of a novel role of IL-13Rα2 in human Glioblastoma multiforme: interleukin-13 mediates signal transduction through AP-1 pathway. *J. Transl. Med.* **16**, 369 (2018).
25. Debinski, W., Gibo, D. M., Hulet, S. W., Connor, J. R. & Gillespie, G. Y. Receptor for interleukin 13 is a marker and therapeutic target for human high-grade gliomas. *Clin. Cancer Res.* **5**, 985–990 (1999).
26. Kawakami, M., Kawakami, K., Takahashi, S., Abe, M. & Puri, R. K. Analysis of interleukin-13 receptor alpha2 expression in human pediatric brain tumors. *Cancer* **101**, 1036–1042 (2004).
27. Li, X. et al. Expression of Interleukin-13 Receptor Alpha 2 in Brainstem Gliomas. *Cancers* **16**, https://doi.org/10.3390/cancers16010228 (2024).
28. Debinski, W., Obiri, N. I., Pastan, I. & Puri, R. K. A novel chimeric protein composed of interleukin 13 and Pseudomonas exotoxin is highly cytotoxic to human carcinoma cells expressing receptors for interleukin 13 and interleukin 4. *J. Biol. Chem.* **270**, 16775–16780 (1995).
29. Debinski, W., Obiri, N. I., Powers, S. K., Pastan, I. & Puri, R. K. Human glioma cells overexpress receptors for interleukin 13 and are extremely sensitive to a novel chimeric protein composed of interleukin 13 and pseudomonas exotoxin. *Clin. Cancer Res.* **1**, 1253–1258 (1995).
30. Souweidane, M. M., Occhiogrosso, G., Mark, E. B. & Edgar, M. A. Interstitial infusion of IL13-PE38QQR in the rat brain stem. *J. Neurooncol.* **67**, 287–293 (2004).
31. Lian, X. et al. Design considerations of an IL13Rα2 antibody-drug conjugate for diffuse intrinsic pontine glioma. *Acta Neuropathol. Commun.* **9**, 88 (2021).

32. Rechberger, J. S. et al. IL-13Rα2 status predicts GB-13 (IL13.E13K-PE4E) efficacy in high-grade glioma. *Pharmaceutics* **14**, https://doi.org/10.3390/pharmaceutics14050922 (2022).
33. Brown, C. E. et al. Bioactivity and safety of IL13Rα2-redirected chimeric antigen receptor CD8+ T cells in patients with recurrent glioblastoma. *Clin. Cancer Res.* **21**, 4062–4072 (2015).
34. Brown, C. E. et al. Regression of glioblastoma after chimeric antigen receptor T-cell therapy. *N. Engl. J. Med.* **375**, 2561–2569 (2016).
35. Brown, C. E. et al. Optimization of IL13Rα2-targeted chimeric antigen receptor T cells for improved anti-tumor efficacy against glioblastoma. *Mol. Ther.* **26**, 31–44 (2018).
36. Vogelbaum, M. A. et al. Convection-enhanced delivery of cintredekin besudotox (interleukin-13-PE38QQR) followed by radiation therapy with and without temozolomide in newly diagnosed malignant gliomas: phase 1 study of final safety results. *Neurosurgery* **61**, 1031–1037 (2007). discussion 1037–1038.
37. Kunwar, S. et al. Phase III randomized trial of CED of IL13-PE38QQR vs Gliadel wafers for recurrent glioblastoma. *Neuro Oncol.* **12**, 871–881 (2010).
38. Chittiboina, P., Heiss, J. D., Warren, K. E. & Lonser, R. R. Magnetic resonance imaging properties of convective delivery in diffuse intrinsic pontine gliomas. *J. Neurosurg. Pediatr.* **13**, 276–282 (2014).
39. Heiss, J. D. et al. Phase I trial of convection-enhanced delivery of IL13-Pseudomonas toxin in children with diffuse intrinsic pontine glioma. *J. Neurosurg. Pediatr.* **23**, 333–342 (2018).
40. Mrowczynski, O. D. et al. Targeting IL-13Rα2 for effective treatment of malignant peripheral nerve sheath tumors in mouse models. *J. Neurosurg.* **131**, 1369–1379 (2018)
41. Jinno, Y. et al. Domain II mutants of Pseudomonas exotoxin deficient in translocation. *J. Biol. Chem.* **264**, 15953–15959 (1989).
42. Chaudhary, V. K., Jinno, Y., Gallo, M. G., FitzGerald, D. & Pastan, I. Mutagenesis of Pseudomonas exotoxin in identification of sequences responsible for the animal toxicity. *J. Biol. Chem.* **265**, 16306–16310 (1990).
43. Puri, R. K. et al. Targeting of interleukin-13 receptor on human renal cell carcinoma cells by a recombinant chimeric protein composed of interleukin-13 and a truncated form of Pseudomonas exotoxin A (PE38QQR). *Blood* **87**, 4333–4339 (1996).
44. Armstrong, S., Yates, S. P. & Merrill, A. R. Insight into the catalytic mechanism of Pseudomonas aeruginosa exotoxin A. Studies of toxin interaction with eukaryotic elongation factor-2. *J. Biol. Chem.* **277**, 46669–46675 (2002).
45. Du, X., Youle, R. J., FitzGerald, D. J. & Pastan, I. Pseudomonas exotoxin A-mediated apoptosis is Bak dependent and preceded by the degradation of Mcl-1. *Mol. Cell. Biol.* **30**, 3444–3452 (2010).
46. Schmidt, M. et al. Synergistic interaction between an anti-p185HER-2 pseudomonas exotoxin fusion protein [scFv(FRP5)-ETA] and ionizing radiation for inhibiting growth of ovarian cancer cells that overexpress HER-2. *Gynecol. Oncol.* **80**, 145–155 (2001).
47. Hassan, R. et al. Tumor-directed radiation and the immunotoxin SS1P in the treatment of mesothelin-expressing tumor xenografts. *Clin. Cancer Res.* **12**, 4983–4988 (2006).
48. Cerami, E. et al. The cBio cancer genomics portal: an open platform for exploring multidimensional cancer genomics data. *Cancer Discov.* **2**, 401–404 (2012).
49. Gao, J. et al. Integrative analysis of complex cancer genomics and clinical profiles using the cBioPortal. *Sci. Signal.* **6**, pl1 (2013).
50. de Bruijn, I. et al. Analysis and visualization of longitudinal genomic and clinical data from the AACR project GENIE biopharma collaborative in cBioPortal. *Cancer Res*. https://doi.org/10.1158/0008-5472.Can-23-0816 (2023).
51. Shapiro, J. A. et al. OpenPBTA: the open pediatric brain tumor atlas. *Cell Genom.* **3**, 100340 (2023).
52. Ianevski, A., Giri, A. K. & Aittokallio, T. SynergyFinder 2.0: visual analytics of multi-drug combination synergies. *Nucleic Acids Res.* **48**, W488–w493 (2020).
53. Zheng, S. et al. SynergyFinder Plus: toward better interpretation and annotation of drug combination screening datasets. *Genom. Proteom. Bioinform.* **20**, 587–596 (2022).
54. Bliss, C. I. The toxicity of poisons applied jointly 1. *Ann. Appl. Biol.* **26**, 585–615 (1939).
55. Loewe, S. The problem of synergism and antagonism of combined drugs. *Arzneim. Forsch.* **3**, 285–290 (1953).
56. Berenbaum, M. C. What is synergy? *Pharm. Rev*. **41**, 93–141 (1989).
57. Yadav, B., Wennerberg, K., Aittokallio, T. & Tang, J. Searching for drug synergy in complex dose-response landscapes using an interaction potency model. *Comput. Struct. Biotechnol. J.* **13**, 504–513 (2015).
58. Guzmán, C., Bagga, M., Kaur, A., Westermarck, J. & Abankwa, D. ColonyArea: an ImageJ plugin to automatically quantify colony formation in clonogenic assays. *PLoS ONE* **9**, e92444 (2014).
59. Djuzenova, C. S. et al. Radiosensitivity in breast cancer assessed by the histone γ-H2AX and 53BP1 foci. *Radiat. Oncol.* **8**, 98 (2013).
60. Chen, J. et al. Aberrant ATM signaling and homology-directed DNA repair as a vulnerability of p53-mutant GBM to AZD1390-mediated radiosensitization. *Sci. Transl. Med.* **16**, eadj5962 (2024).
61. Ji, J. et al. Differential distribution of the DNA-PKcs inhibitor peposertib selectively radiosensitizes patient-derived melanoma brain metastasis xenografts. *Mol. Cancer Ther*. https://doi.org/10.1158/1535-7163.Mct-23-0552 (2024).
62. Power, E. A. et al. Overcoming translational barriers in H3K27-altered diffuse midline glioma: Increasing the drug-tumor residence time. *Neurooncol. Adv.* **5**, vdad033 (2023).
63. Larson, J. D. et al. Histone H3.3 K27M accelerates spontaneous brainstem glioma and drives restricted changes in bivalent gene expression. *Cancer Cell* **35**, 140–155.e147 (2019).
64. Morales La Madrid, A. et al. Second re-irradiation for DIPG progression, re-considering “old strategies” with new approaches. *Childs Nerv. Syst.* **33**, 849–852 (2017).
65. Gallitto, M. et al. Role of radiation therapy in the management of diffuse intrinsic pontine glioma: a systematic review. *Adv. Radiat. Oncol.* **4**, 520–531 (2019).
66. Aziz-Bose, R. & Monje, M. Diffuse intrinsic pontine glioma: molecular landscape and emerging therapeutic targets. *Curr. Opin. Oncol.* **31**, 522–530 (2019).
67. van den Bent, M., Saratsis, A. M., Geurts, M. & Franceschi, E. H3 K27M-altered glioma and diffuse intrinsic pontine glioma: semi-systematic review of treatment landscape and future directions. *Neuro Oncol*. https://doi.org/10.1093/neuonc/noad220 (2023).
68. Pandey, K. et al. A combined immunopeptidomics, proteomics, and cell surface proteomics approach to identify immunotherapy targets for diffuse intrinsic pontine glioma. *Front. Oncol.* **13**, 1192448 (2023).
69. Sampson, J. H. et al. Poor drug distribution as a possible explanation for the results of the PRECISE trial. *J. Neurosurg.* **113**, 301–309 (2010).
70. Mueller, S. et al. Effect of imaging and catheter characteristics on clinical outcome for patients in the PRECISE study. *J. Neurooncol.* **101**, 267–277 (2011).
71. Shi, M. & Sanche, L. Convection-enhanced delivery in malignant gliomas: a review of toxicity and efficacy. *J. Oncol.* **2019**, 9342796 (2019).
72. Rechberger, J. S. & Daniels, D. J. Locoregional infusion of IL13Rα2-specific immunotoxins in children and adults with high-grade glioma. *Ther. Deliv*. https://doi.org/10.4155/tde-2022-0019 (2022).
73. Bartolomé, R. A. et al. IL13 receptor α2 signaling requires a scaffold protein, FAM120A, to activate the FAK and PI3K pathways in colon cancer metastasis. *Cancer Res* **75**, 2434–2444 (2015).

74. Kioi, M., Kawakami, M., Shimamura, T., Husain, S. R. & Puri, R. K. Interleukin-13 receptor alpha2 chain: a potential biomarker and molecular target for ovarian cancer therapy. *Cancer* **107**, 1407–1418 (2006).
75. Fujisawa, T., Joshi, B., Nakajima, A. & Puri, R. K. A novel role of interleukin-13 receptor alpha2 in pancreatic cancer invasion and metastasis. *Cancer Res.* **69**, 8678–8685 (2009).
76. Okamoto, H. et al. Interleukin-13 receptor α2 is a novel marker and potential therapeutic target for human melanoma. *Sci. Rep.* **9**, 1281 (2019).
77. Morgan, R. N., Saleh, S. E., Farrag, H. A. & Aboshanab, K. M. New insights on Pseudomonas aeruginosa exotoxin A-based immunotoxins in targeted cancer therapeutic delivery. *Ther. Deliv.* **14**, 31–60 (2023).
78. Dieffenbach, M. & Pastan, I. Mechanisms of resistance to immunotoxins containing pseudomonas exotoxin A in cancer therapy. *Biomolecules* **10**, https://doi.org/10.3390/biom10070979 (2020).
79. Santajit, S. et al. Human single-chain antibodies that neutralize Pseudomonas aeruginosa-exotoxin A-mediated cellular apoptosis. *Sci. Rep.* **9**, 14928 (2019).
80. Husain, S. R., Joshi, B. H. & Puri, R. K. Interleukin-13 receptor as a unique target for anti-glioblastoma therapy. *Int. J. Cancer* **92**, 168–175 (2001).
81. Kawakami, M., Kawakami, K. & Puri, R. K. Intratumor administration of interleukin 13 receptor-targeted cytotoxin induces apoptotic cell death in human malignant glioma tumor xenografts. *Mol. Cancer Ther.* **1**, 999–1007 (2002).
82. Husain, S. R. & Puri, R. K. Interleukin-13 receptor-directed cytotoxin for malignant glioma therapy: from bench to bedside. *J. Neurooncol.* **65**, 37–48 (2003).
83. Matt, S. & Hofmann, T. G. The DNA damage-induced cell death response: a roadmap to kill cancer cells. *Cell Mol. Life Sci.* **73**, 2829–2850 (2016).
84. Mladenov, E., Magin, S., Soni, A. & Iliakis, G. DNA double-strand break repair as determinant of cellular radiosensitivity to killing and target in radiation therapy. *Front. Oncol.* **3**, 113 (2013).
85. Kawakami, K., Kawakami, M., Liu, Q. & Puri, R. K. Combined effects of radiation and interleukin-13 receptor-targeted cytotoxin on glioblastoma cell lines. *Int. J. Radiat. Oncol. Biol. Phys.* **63**, 230–237 (2005).
86. Bromley, R., Oliver, L., Davey, R., Harvie, R. & Baldock, C. Predicting the clonogenic survival of A549 cells after modulated X-ray irradiation using the linear quadratic model. *Phys. Med. Biol.* **54**, 187–206 (2009).
87. Franken, N. A. et al. Cell survival and radiosensitisation: modulation of the linear and quadratic parameters of the LQ model (Review). *Int. J. Oncol.* **42**, 1501–1515 (2013).
88. Mamo, T. et al. Inhibiting DNA-PK(CS) radiosensitizes human osteosarcoma cells. *Biochem. Biophys. Res. Commun.* **486**, 307–313 (2017).
89. Masilamani, A. P. et al. An anti-PSMA immunotoxin reduces Mcl-1 and Bcl2A1 and specifically induces in combination with the BAD-Like BH3 mimetic ABT-737 apoptosis in prostate cancer cells. *Cancers* **12**, https://doi.org/10.3390/cancers12061648 (2020).
90. Noll, T., Schultze-Seemann, S., Kuckuck, I., Michalska, M. & Wolf, P. Synergistic cytotoxicity of a prostate cancer-specific immunotoxin in combination with the BH3 mimetic ABT-737. *Cancer Immunol. Immunother.* **67**, 413–422 (2018).
91. Tosi, U. & Souweidane, M. Diffuse midline gliomas: challenges and new strategies in a changing clinical landscape. *Cancers* **16**, https://doi.org/10.3390/cancers16010219 (2024).
92. Welby, J. P. et al. Current murine models and new developments in H3K27M diffuse midline gliomas. *Front Oncol.* **9**, 92 (2019).
93. Chen, Z. et al. Advanced pediatric diffuse pontine glioma murine models pave the way towards precision medicine. *Cancers* **13**, https://doi.org/10.3390/cancers13051114 (2021).
94. Koschmann, C. et al. A road map for the treatment of pediatric diffuse midline glioma. *Cancer Cell* **42**, 1–5 (2024).
95. Misuraca, K. L., Cordero, F. J. & Becher, O. J. Pre-clinical models of diffuse intrinsic pontine glioma. *Front. Oncol.* **5**, 172 (2015).
96. Vitanza, N. A. & Monje, M. Diffuse intrinsic pontine glioma: from diagnosis to next-generation clinical trials. *Curr. Treat. Options Neurol.* **21**, 37 (2019).
97. Mueller, S. et al. Consensus framework for conducting phase I/II clinical trials for children, adolescents, and young adults with pediatric low-grade glioma: Guidelines established by the International Pediatric Low-Grade Glioma Coalition Clinical Trial Working Group. *Neuro Oncol.* **26**, 407–416 (2024).
98. Chen, Y., Zhao, C., Li, S., Wang, J. & Zhang, H. Immune Microenvironment and Immunotherapies for Diffuse Intrinsic Pontine Glioma. *Cancers* **15**, https://doi.org/10.3390/cancers15030602 (2023)
99. Lieberman, N. A. P. et al. Characterization of the immune microenvironment of diffuse intrinsic pontine glioma: implications for development of immunotherapy. *Neuro Oncol.* **21**, 83–94 (2019).
100. Persson, M. L. et al. The intrinsic and microenvironmental features of diffuse midline glioma: Implications for the development of effective immunotherapeutic treatment strategies. *Neuro Oncol.* **24**, 1408–1422 (2022).
101. Geng, Z. et al. The open pediatric cancer project. *bioRxiv*. https://doi.org/10.1101/2024.07.09.599086 (2024).
102. Zhang, L. et al. STAT3 is a biologically relevant therapeutic target in H3K27M-mutant diffuse midline glioma. *Neuro Oncol.* **24**, 1700–1711 (2022).
103. Maigne, L. et al. CPOP: An open source C++ cell POPulation modeler for radiation biology applications. *Phys. Med.* **89**, 41–50 (2021).
104. Nagaraja, S. et al. Transcriptional dependencies in diffuse intrinsic pontine glioma. *Cancer Cell* **31**, 635–652.e636 (2017).
105. Grasso, C. S. et al. Functionally defined therapeutic targets in diffuse intrinsic pontine glioma. *Nat. Med.* **21**, 555–559 (2015).
106. Katzung, B. G. Basic and Clinical Pharmacology. *McGraw-Hill Medical* (2012).
107. Dobin, A. et al. STAR: ultrafast universal RNA-seq aligner. *Bioinformatics* **29**, 15–21 (2013).
108. Li, B. & Dewey, C. N. RSEM: accurate transcript quantification from RNA-Seq data with or without a reference genome. *BMC Bioinform.* **12**, 323 (2011).
109. Tang, J., Wennerberg, K. & Aittokallio, T. What is synergy? The Saariselkä agreement revisited. *Front Pharm.* **6**, 181 (2015).
110. Tang, J. Informatics approaches for predicting, understanding, and testing cancer drug combinations. *Methods Mol. Biol.* **1636**, 485–506 (2017).
111. Carlson, B. L., Pokorny, J. L., Schroeder, M. A. & Sarkaria, J. N. Establishment, maintenance and in vitro and in vivo applications of primary human glioblastoma multiforme (GBM) xenograft models for translational biology studies and drug discovery. *Curr. Protoc. Pharmacol.* **Chapter 14**, Unit 14.16. https://doi.org/10.1002/0471141755.ph1416s52 (2011)
112. Paxinos, G. & Watson, C. *The Rat Brain In Stereotaxic Coordinates: Hard Cover Edition* (Elsevier, 2006).
113. van Hoof, S. J., Verde, J. B. & Verhaegen, F. Dose painting by dynamic irradiation delivery on an image-guided small animal radiotherapy platform. *Br. J. Radio.* **92**, 20180744 (2019).
114. Cardiff, R. D., Miller, C. H. & Munn, R. J. Manual hematoxylin and eosin staining of mouse tissue sections. *Cold Spring Harb. Protoc.* **2014**, 655–658 (2014).

115. Hu, Y. & Smyth, G. K. ELDA: extreme limiting dilution analysis for comparing depleted and enriched populations in stem cell and other assays. *J. Immunol. Methods* **347**, 70–78 (2009).

Acknowledgements

The authors gratefully thank Suzanne Baker (St. Jude Children's Research Hospital) and Michelle Monje (Stanford University) for use of the GEMM animal model and the SU-DIPG XIII-P cell line, respectively. Furthermore, we acknowledge the generous support of Jann Sarkaria, Shiv Gupta, Ann Mladek, Brett Carlson (Mayo Clinic). We also acknowledge our medical illustrator, Stephen Graepel, for outstanding illustrations of the study design and experimental workflow. Additional figures were created using BioRender.com. This work was supported by the Small Business Innovation Research (SBIR) and Small Business Technology Transfer (STTR) programs (CA275560-01). Data in this publication were produced in the Mayo Clinic Pathology Research Core (PRC) which is supported by the Mayo Clinic Comprehensive Cancer Center Grant, funded by National Cancer Institute (P30CA15083).

Author contributions

J.S.R., L.Z., D.J.D. designed research; J.S.R., W.J.F.V., L.F.N., J.G., R.S.S., L.Z., D.J.D. performed research; J.S.R., W.J.F.V., L.F.N., R.S.S., R.A.V., L.Z., D.J.D. analyzed data; and J.S.R., L.Z., D.J.D. wrote the paper.

Competing interests

The authors declare no competing interests.

Additional information

Supplementary information The online version contains supplementary material available at https://doi.org/10.1038/s42003-025-09155-9.

Correspondence and requests for materials should be addressed to David J. Daniels.

Peer review information *Communications Biology* thanks Anthony Wang, Oren Becher, and the other, anonymous, reviewer for their contribution to the peer review of this work. Primary Handling Editors: Kaliya Georgieva.

Reprints and permissions information is available at http://www.nature.com/reprints